Initial report on statistical separability of vegetation and bottom types in laser data

MICHAEL TULLDAHL, SOFIA WIKSTRÖM

FOI, Swedish Defence Research Agency, is a mainly assignment-funded agency under the Ministry of Defence. The core activities are research, method and technology development, as well as studies conducted in the interests of Swedish defence and the safety and security of society. The organisation employs approximately 1000 personnel of whom about 800 are scientists. This makes FOI Sweden's largest research institute. FOI gives its customers access to leading-edge expertise in a large number of fields such as security policy studies, defence and security related analyses, the assessment of various types of threat, systems for control and management of crises, protection against and management of hazardous substances, IT security and the potential offered by new sensors.

FOI
Defence Research Agency
Information Systems
P.O. Box 1165
SE-581 11 Linköping

Phone: +46 13 37 80 00
Fax: +46 13 37 81 00

www.foi.se

FOI-R--2961--SE Technical report
ISSN 1650-1942 January 2010

Information Systems

Michael Tulldahl, Sofia Wikström

Initial report on statistical separability of vegetation and bottom types in laser data

Titel	Statistisk separerbarhet mellan vegetation och bottentyper i laserdata - Inledande rapport
Title	Initial report on statistical separability of vegetation and bottom types in laser data

Rapportnr/Report no	FOI-R--2961--SE
Rapporttyp Report Type	Teknisk rapport Technical report
Sidor/Pages	51 p
Månad/Month	January
Utgivningsår/Year	2010
ISSN	ISSN 1650-1942
Kund/Customer	Naturvårdsverket
Projektnr/Project no	B53008
Godkänd av/Approved by	Johan Allgurén

FOI, Totalförsvarets Forskningsinstitut	FOI, Swedish Defence Research Agency
Avdelningen för Informationssystem	Information Systems
Box 1165	P.O. Box 1165
581 11 Linköping	SE-581 11 Linköping

Sammanfattning

Flygburen laserskanning är sedan ett tiotal år en operativ teknik för mätning av bottendjup. Ett av de operativa systemen för djupsondering är Hawk Eye II-systemet. I denna rapport undersöks möjligheter att klassificera vegetation och substrat genom att experimentellt studera separerbarhet i laserdata från olika bottentyper. Vi studerar ett antal variabler ur data från Hawk Eye II-systemet, vilka har potential att beskriva bottnens reflektivitet och ojämnhet. Dessa variabler extraheras ur pulssvaret, även kallat vågformen, som mottagits efter att laserns puls reflekterats av vattenvolym och botten. I rapporten beskrivs även metoder för att korrigera variablerna för djup, vattnets grumlighet och ett antal lasersystemberoende parametrar.

De korrigerade variablerna studeras över fältytor som inventerats med undervattensvideofilmning. Variablerna undersöks separat, samt kombineras med varandra och med djupdata från lasersystemet för testklassificering av de fyra olika bottentyperna Sand, Låg vegetation (*Zostera marina*), Hög vegetation (*Potamogeton perfoliatus*) och Block. Med den bästa kombinationen av vågformsvariabler och variabler skattade från djupdata uppnåddes en klassificeringsnoggrannhet på ca 70 % mellan dessa bottentyper. Resultaten visar att vågformsvariablerna har en stor potential att förbättra klassningen av substrat och vegetation jämfört med att enbart använda djupdata.

Denna rapport beskriver det inledande arbetet inom EMMA-programmet (Environmental Mapping and Monitoring with Airborne laser and digital images). De preliminära metoderna och resultaten i detta arbete kommer att vidareutvecklas och undersökas med laser- och fältdata från flera platser.

Nyckelord: Laserskanning, lidar, klassificering, vegetation, vågform

Summary

During the last decade, airborne laser scanning has developed into an operational technique for bathymetric mapping. One of the operational systems for depth sounding is the Hawk Eye II system. In this report, we examine the possibilities for classification of bottom vegetation and substrates by experimental evaluation of the separability in laser data between different bottom types. We study a number of data variables from the Hawk Eye II system, which have the potential to describe the reflectivity and the roughness of the sea bottom. These variables are extracted from the pulse response, also denoted the waveform, of the emitted and reflected laser pulse from the water volume and the sea bottom. We also describe methods for correction of the waveform variables for depth, water turbidity, and laser system parameters.

The corrected variables are studied over field patches which were documented by underwater video. The variables are evaluated separately, in combination with each other, and combined with laser depth data for test classification of the four bottom types Sand, Low Vegetation (*Zostera marina*), High Vegetation (*Potamogeton perfoliatus*) and Boulders. With the best combination of waveform variables and variables calculated from depth data, a total classification accuracy of about 70 % was obtained between these bottom types. Our results show that the waveform variables have a potential for significant improvement of the classification accuracy compared to when only depth data is used for classification of bottom substrates and vegetation.

This report describes the initial work in the EMMA programme (Environmental Mapping and Monitoring with Airborne laser and digital images). The preliminary methods and results presented in this report will be further evaluated and developed using laser data and field data from several sites.

Keywords: Laser scanning, lidar, classification, vegetation, waveform

Table of contents

1 Introduction

During the last decade, airborne laser scanning has developed into an operational technique. Several national, regional and local administrations are planning laser surveys of shallow waters for generation of depth data. One of the operational systems is the Swedish Hawk Eye II, which operates in both green (for water depth) and NIR wavelengths (for land/coastal topography). The full waveform of the retrieved laser signal is captured and aerial digital images are simultaneously recorded by the system. There is thus the potential to retrieve information about bottom vegetation as well, but this information is currently not interpreted. The lack of such data is fundamental in the marine systems. Here, both good bottom topography maps as well as estimates of the areal distribution of plant (and animal) communities is totally lacking, except for a few sites that have been covered by divers' investigations, video-mapping or attempts to interpret aerial photography taken over the most shallow areas.

Laser scanning for characterisation of marine environments is increasingly gaining interest. In the intertidal zone, topographic features mapped with lidar (e.g. elevation, slope and aspect) have been used to map seabed substratum types[1] and vegetation.[2, 3] Chust *et al.*[3] demonstrated that adding reflectivity of the lidar signal improved the accuracy of the habitat classification, compared to using only the topographic information. Less work has been done to map habitats or vegetation in the subtidal. Here, an additional challenge is to account for the effect of water column above the seabed on the lidar signal. Tuell *et al.*[4, 5] have demonstrated the potential to produce estimates of green laser reflectance and optical properties of the water column by analyzing laser waveforms; this in turn provides for the fusion of laser, multi- and hyper-spectral digital imaging for classification of sea floor vegetation. Wang and Philpot[6] managed to produce a map of sand, continuous seagrass, and discontinuous seagrass using waveform variables. Vegetation classification from laser bathymetry waveform data in less clear coastal waters was made by Tulldahl *et al.*,[7, 8] where an overall classification accuracy of greater than 80%[7] was obtained compared to field data for eelgrass, sand, and dark algae.

Compared to earlier work, we have in this report examined a larger number of different features extracted from the bottom echo of the lidar waveform. These features include information about both the bottom roughness and reflectivity. To our knowledge, earlier work has only attempted to extract reflectivity data from the waveform, with the exception of Refs. [7, 8]. Our work also includes the use of field data of bottom substrates and vegetation which is rare in earlier work published in the subject of bottom classification from airborne lidar data.

We have used laser data from a survey made in 2007 with the Hawk Eye II system, together with field data from underwater video, geo-referenced using conventional GPS. The video data was captured on two occasions, the first occasion the same day as the lidar survey and the second two years later. The video data was recorded over randomly chosen transects distributed over the lidar survey site. By manual interpretation of the video data we generated observation patches which each included estimations of substrates and species cover. Also, the patch size was estimated over which the cover conditions were similar within the patch. From the interpreted video data a set of 18 patches were chosen for studies of variables from the laser data. The bottom depths in these patches were between 3 and 11 m. We have studied several variables extracted from the lidar waveform or calculated from the lidar depth data. These variables describe either the bottom reflectivity, roughness, or a mix of both. For analysis of separability a subset of 9 patches, within the depth interval 3 m - 7 m, was chosen which had high coverage of one single vegetation or substrate. The analysis included four bottom types; Sand, Low Vegetation, High Vegetation and Boulders. The separability analysis was performed with classification tests, where the classification accuracy was evaluated for different combinations of classification variables. The classification was made with a multivariate method using averages and covariance matrices of the variables studied.

One purpose with this report is to obtain preliminary results of species and substrate separability using airborne bathymetric laser data, where not only depth data is used but also information from the full lidar waveform. A second purpose is to define a basic set of lidar waveform features and to develop accurate methods for correction of these features.

This report is a part of the work in the EMMA programme (Environmental Mapping and Monitoring with Airborne laser and digital images). The preliminary results and methods in this report will be used in our continued work where the methods will be further evaluated and developed using lidar and field data from several sites. Our future work will also include development of classification methods for combined use of lidar and aerial imagery data.

In the following sections we present the field data (Section 2), the Hawk Eye II lidar system (Section 3) and the waveform variables (Section 4). In Section 5 the classification method and results are presented and discussed. Several factors such as the water surface and the water volume between the sensor and the sea floor require that accurate corrections of the extracted waveform features are applied. These correction methods are presented in Appendix A of the report.

2 Test Site and Field Inventory Data

The study was performed in the Arkö Archipelago in the Baltic Sea Proper (Fig. 1). The Baltic Sea is a large area of brackish water with constantly low salinity (around 7 psu in the study area). The study area is typical for the Swedish coast of the Baltic Sea, with an archipelago of islands and skerries. The bottom substrate is a complex mixture of bedrock and glacial and postglacial deposits. Typically, bedrock, stones and boulders dominates in areas where sediment is washed away, i.e. in shallow areas exposed to waves or currents and where the bottom is steep. Fine sediment (sand and mud) is accumulated in deep and sheltered areas.

The vegetation consists of a mosaic of macroalgal communities on hard substrates and phanerogams and stoneworts on soft substrates. The macroalgal vegetation is dominated by small species. The largest species, bladder wrack (*Fucus vesiculosus*), only occasionally reaches a size of 1 m. Large kelp species are lacking due to the low salinity. The vegetation is usually dense, covering all available hard substrate. The vegetation on soft substrate include a large diversity of species with different morphology and varies from very dense to sparse and from low (e.g. stoneworts) to several meters height (most notably *Potamogeton perfoliatus*).

The Arkö Archipelago is situated close to the outlet of Motala Ström (in Norrköping, Fig. 1), a watercourse with a large catchment area transporting large amounts of nutrients and humic substances into the Baltic Sea. This is reflected by a smaller Secchi depth in this area compared to other archipelago areas in the region (up to 2 m smaller Secchi depths in August). The Secchi depths measured the same day as the lidar survey was 5-6 m (measured at six locations dispersed over the area covered by lidar).This is reasonably good in a coastal area of the Baltic Sea, but Secchi depths larger than 8 m has been recorded in adjacent archipelago areas in August (www.motalastrom.org/arsrapporter/2008/alcontrol/PDFer/StoraMSV2008.pdf). The attenuation coefficient c at wavelength 532 nm was between 0.75 m^{-1} and 0.85 m^{-1} (measured with a c-Beta instrument from HobiLabs Inc. on the same day and locations as the Secchi depths).

Field data for training and validation of the classification model was collected with underwater video. The main part of the data was collected on October 18 2007, the same day as the lidar survey. Data was recorded in 52 patches dispersed over the test site. The patches varied in size from 2x3 to 6x3 m. In addition, we used data from investigations in August 2008 and 2009, where randomly chosen patches (5x5 m) were investigated using similar video equipment. This added another 13 patches (6 from 2008 and 7 from 2009) that were within the area covered by the lidar survey. Including data from different time periods potentially introduces an error in the analyses since the vegetation can change both between years and seasons. In this case, we expect the main vegetation that was found in the patches from 2008 and 2009 to be relatively stable between years.

In each patch, the degree cover of each species was estimated using a 7-grade scale (1, 5, 10, 25, 50, 75 and 100 % cover). In addition, bottom substratum (cover of rock, boulders, stones, pebbles, sand and soft substratum) was estimated using the same 7-grade scale.

Of the total 65 patches from 2007, 2008, and 2009, a subset of patches was chosen based on the following criteria: the degree cover of species and substratum could be done reliably; the number of different substrates and species should be limited; the bottom depth should be less than 12 m which was the approximate maximum depth limit for the lidar data; and the bottom slope angle within the patch should be less than 20 degrees. The remaining subset matching the criteria contained 18 patches which are listed in Table 1. Of these patches, only those with a homogenous substrate and vegetation were included in the multivariate analyses of separability. We further excluded the patches with homogenous mud from these analyses since they are at the limit of the maximum lidar depth range (see Subsection 5.1). The remaining patches were grouped according to substrate and

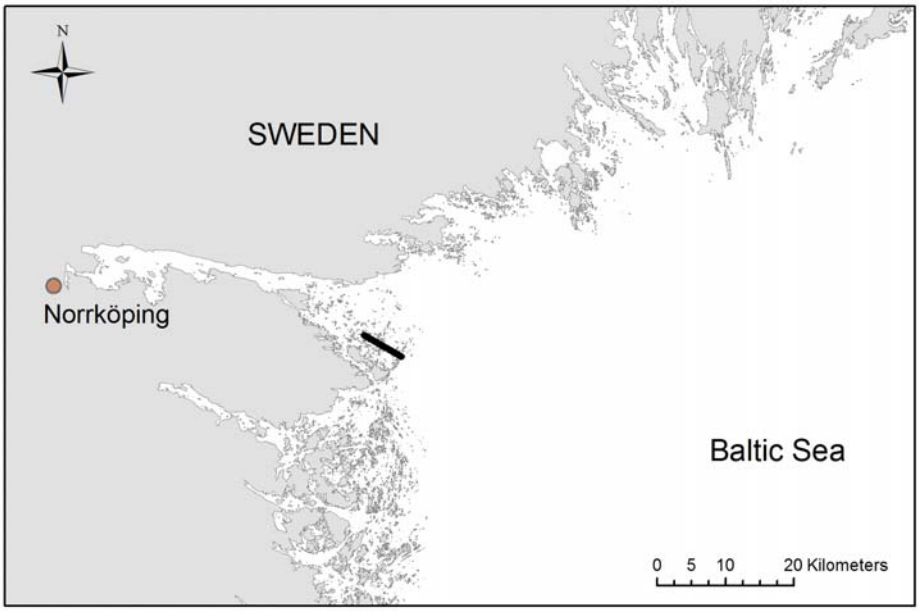

Fig. 1. Overview of the location of the test site. The lidar survey area, approximately 7 km by 0.5 km, is marked with a black line.

vegetation into the classes *Sand*, *High Vegetation*, *Low Vegetation*, and *Boulders*, as shown in the right part of Table 1. All 18 patches in Table 1 are used in visualisation of single classification variables extracted from lidar data. The bottom depth within each patch, taken from lidar data, is shown in Fig. 2.

One limitation of the field data is that in most cases, patches with a certain bottom substratum and vegetation are situated more closely together than to patches with a different substratum and vegetation. Further, the depth within the patches is more similar within than between bottom types (Fig. 2) and one of the vegetation types in the separability analyses (Low Vegetation) was only found in patches surveyed in 2009. This limits the generality of the conclusions that can be drawn from the present study. This study should therefore be seen as very preliminary and the results should be confirmed using a larger and better designed set of field data.

One experience from this study is that the way the data is collected is a key to the success of the subsequent lidar classification. There are a number of criteria that should be met for a patch to be included in the analyses. One solution is to collect a very large dataset and accept that a large part of the data will not be suitable for the analyses (only 9 of the 65 patches was used in the present separability study). An alternative solution is to choose field patches carefully and only include patches with a slope less than some critical value and patches that have a large spatial extent of homogenous substrate and vegetation. The patches of all bottom types should further be distributed well spatially and across depth categories.

Table 1. Field patches used in the analyses.

ID	Label	Year	Substrate	Vegetation, animals and detritus	Separabilility analysis	
					Label	**ExtVal**
22	$S_{sand,det50,1}$	2007	100% sand	50% detritus	Sand	train
24	$S_{sand,det50,2}$	2007	100% sand	50% detritus	Sand	val
910	$S_{sand,zost75}$	2009	100% sand, 1% stones	75% *Zostera marina*, 5% *Potamogeton pectinatus*, 5% *Mytilus* sp., 1% *Chorda filum*	LowVeg	train
911	$S_{sand,zost75,ppec25}$	2009	100% sand	75% *Zostera marina*, 25% *Potamogeton pectinatus*, 5% *Mytilus* sp.	LowVeg	val
912	$S_{sand,myt25,zan25,fil10}$	2009	100% sand, 1% stones	25% *Mytilus* sp., 25% *Zannichellia marina*, 10% filamentous algae		
38	$S_{sand,pper75,1}$	2007	100% sand	75% *Potamogeton perfoliatus*	HighVeg	train
39	$S_{sand,pper75,2}$	2007	100% sand	75% *Potamogeton perfoliatus*	HighVeg	train
40	$S_{sand,pper75,3}$	2007	100% sand	75% *Potamogeton perfoliatus*	HighVeg	val
42	$S_{sand,pper25,fuc10}$	2007	100% sand, 10% stone	25% *Potamogeton perfoliatus*, 10% *Fucus vesiculosus*		
43	$S_{sand,pper25,fuc10,ppec10}$	2007	100% sand, 10% stone	25% *Potamogeton perfoliatus*, 10% *Potamogeton pectinatus*, 10% *Fucus vesiculosus*		
11	$S_{boul,fil50,myt10}$	2007	100% boulders	50% filamentous algae, 10% *Mytilus* sp.	Boulders	train
12	$S_{boul,fil50,myt50}$	2007	100% boulders	50% filamentous algae, 50% *Mytilus* sp.	Boulders	val
913	$S_{sto50,boul25,gru25,myt25,fil25}$	2009	50% stones, 25% boulders, 25% gravel	25% *Mytilus* sp, 25% filamentous algae, 5% *Furcellaria fastigiata*		
2	$S_{mud,1}$	2007	100% mud	-		
6	$S_{mud,2}$	2007	100% mud	-		
7	$S_{mud,3}$	2007	100% mud	-		
921	$S_{mud,myt25,det10}$	2009	100% mud	25% *Mytilus* sp., 10% detritus		
922	$S_{mud50,sand50,det50}$	2009	50% mud, 50% sand, 1% stone	50% detritus, 5% *Mytilus* sp., 1% *Chorda filum*		

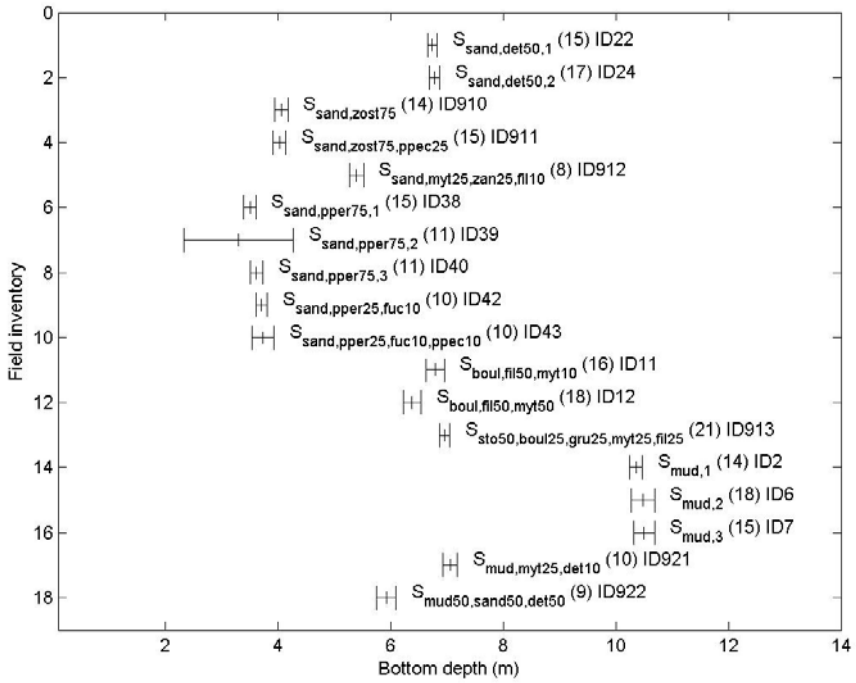

Fig. 2. Depth distribution of the field data patches. For each patch the average and standard deviation of the depth within a radius of 3 m from the centre of the patch is shown.

3 Hawk Eye II System and Lidar Data

The results presented in this report are based on lidar data from a survey with the HawkEye II system in October 18, 2007. The HawkEye II – Airborne coastal survey system, by Airborne Hydrography AB (AHAB), Sweden, consists of the latest advances within airborne bathymetric and topographic lidar technologies (www.airbornehydro.com). The system surveys both land and sea floor simultaneously. Hence, a HawkEye II survey delivers a seamless transition between land and sea-floor from one single survey. The system is operated by one single operator when airborne. Beside the operator, the crew consists of the pilot and a co-pilot who also acts as a spotter supporting the survey. The ground support consists of survey planning, data post processing and quality control. All data and the mission planning are saved on portable devices.

The Hawk Eye II system has a total system weight of less than 180 kg (including wiring) and has a power consumption of less than 1.4 kW. The system is designed for easy installation into most small to medium sized rotary or fixed wing aircraft. The time required for installation in the aircraft is less than an hour. The interfaces necessary from the aircraft are a 28 V power supply, a GPS antenna connection, a mechanical attachment plate, and a photogrammetric window.

The system uses a pulsed, infrared (1064 nm) and green (532 nm) laser for the bathymetric sounding. The infrared pulses are reflected at the water surface whereas the green pulses proceed into the water volume. The laser light backscattered from the sea surface, the water volume and the sea floor is collected in multiple, high-sensitivity receivers. The received waveforms are digitized for further processing and the depth is determined by the time lapse between surface and the bottom echoes. The integrated differential GPS enables positioning of surface, sea floor, and objects in the water column in 3 dimensions in WGS 84 coordinates. The Hawk Eye II system is equipped with a two axis, servo-controlled, scanner mirror to space the sounding spots evenly on the surface. This feature also compensates for flight deviations in yaw, pitch, roll, side slip, speed and altitude. The nominal system optical axis incidence angle from the vertical is 15°-20°. The Hawk Eye II system simultaneously collects 4 kHz bathymetric, 64 kHz topographic lidar soundings and one digital image per second. The sounding spot density for bathymetric data is programmable from 0.5 m x 0.5 m to 3 m x 3 m depending on survey requirements. The flight altitude is between 200 m and 450 m. The swath width of the system is typically 0.2-0.6 times the altitude and the aircraft speed typically 120-180 knots. The area coverage per hour is dependent of parameters such as the turn around time between different flight lines, geometrical shape of the survey area, and requirements of survey accuracy. The Hawk Eye II high laser sounding frequency and the programmable spot density allows high area coverage combined with accurate survey data collection. The system compensations for flight deviations allow for minimized overlap between adjacent flight lines. Since the system simultaneously collects data both above and below the surface only a single mission is required also in complex shallow coastal areas.

The Hawk Eye II system Operator Console software is used both for survey planning and for airborne operation. The software is installed in a portable laptop which is easily connected to the system when airborne. All system parameters can be modified and supervised during the survey via the Operator Console. The software includes an extensive range of tools such as: coverage plots, real time 3-D views of the surveyed area, flight line plan, background map, system parameters, laser pulse responses, and depth ranges. Many attributes are stored for each sounding as a basis for further analysis, post processing, and quality control. The data is stored on hard disks transported from the aircraft for further post processing. In brief, the post processing consists of:

- Refinement of position data with use of navigation post processing software and data from reference stations.

- Analysis of Hydrographic and Topographic elevation data by the AHAB Coastal Survey Studio (CSS) software. The CSS tool includes several advanced algorithms for sub-surface objects detection and identification, quality checks of data, estimates of water and sea floor parameters and decision support to the data cleaning process and interfaces to third party software.
- A cleaning process which includes quality check of the data and removal of faulty data points.
- Further post processing by third party commercially available software or the Coastal Survey Studio depending on the end user requirements for visualization.

The accuracy of the lidar system is very good both for topographic and bathymetric measurements lidar. To reach the best possible absolute accuracy, the dataset is calibrated by data from reference stations and by accurate absolute measurement on specific spots in the survey area. By usage of such reference positions, absolute errors can be reduced from the lidar dataset such that only statistical errors remain. Such procedures result in a very high absolute accuracy of the lidar dataset. In a validation measurement of the statistical accuracy of the Hawk Eye II system a repeatability survey study was performed on the Norwegian coast. A several square kilometres area was surveyed. The survey area included some small islands and a seabed with depths down to 30 meters. The area was surveyed twice on two different days in January 2006. The two datasets were then compared in order to conclude the accuracy of the HawkEye II bathymetric lidar data. The average depth differences between the datasets in these tests were below 5 cm for all depths down to 30 meters. The average position error of the data from the Hawk Eye II system can be as low as one metre under good conditions, and depends on the quality of the data from the reference stations and environmental factors.

In this study we have used data from a Hawk Eye II survey performed by Blom Aerofilms Ltd (http://www.blom.no/aerofilms/en, http://www.topeye.com/sweden/en) in the Arkö Archipelago in the Baltic Sea Proper in October 18, 2007. The depth data used were post processed and quality checked by Blom Aerofilms Ltd. In our additional post-processing we explore further use of information from the time-resolved waveform.

4 Classification Variables from Laser Data

Sea floor classification algorithms can use characteristics from the received lidar waveform and other information obtained from the lidar data such as the bottom slope angle. An example of a waveform from the HawkEye II system is shown in Fig. 3 (a). We calculate the waveform characteristics of the bottom echo pulse from the *difference wave* (Fig. 3 (b)-(c)), which is calculated as the difference between the waveform, in linear scale, and an interpolated volume backscatter wave under the bottom echo according to Refs. [9] and [10]. The basic principle for estimation of the bottom depth is by measuring the time lapse between the surface echo and the 50% level on the leading edge of the bottom echo, see in Fig. 3 (d). An example of a waveform feature that can be used for bottom classification is the width of the bottom echo pulse. From earlier experiments[8, 11] and simulations [10, 12] we have experienced that small objects on the sea bottom can be detected by an increase in the reflected bottom pulse width. The bottom pulse width can also be used for indication of elevated vegetation on the sea floor.

In Fig. 4 we show schematic descriptions of a basic set of bottom echo features. These features are extracted from the bottom echo difference wave. A necessary step is to correct these features to *classification variables* that can be used for classification of the sea floor. The water volume and water surface between the sensor and the sea floor require that accurate corrections are applied. Using simulated waveform data, we have made correction models for each of the waveform features. The correction models include effects from e.g. the water turbidity, the bottom depth and the flight altitude. The purpose of the models is to remove effects from the water volume and water surface to obtain pulse data which mainly are influenced by the bottom type or vegetation. A description of the correction models is given in Appendix 1. In Fig. 5 the notation for our corrected classification variables is described. In this notation:

- Variables VS and VD refer to corrected *waveform* variables from the HawkEye II *shallow* and *deep* channels respectively.
- Variables VB refer to variables derived from the *bottom depth data* in the vicinity of a specific geographic position.
- The subscripts *refl*, *rough* or *mix* refer to waveform variables that can be physically connected to bottom substrate or vegetation *reflectance, roughness,* or a *mix* of both.
- The subscripts *res* and *rat* refer to whether the correction is of *residual* or *ratio* type (Appendix A).
- The subscript *N* denotes that the variable was normalised with respect to the standard deviation of the corresponding correction model (Appendix A).

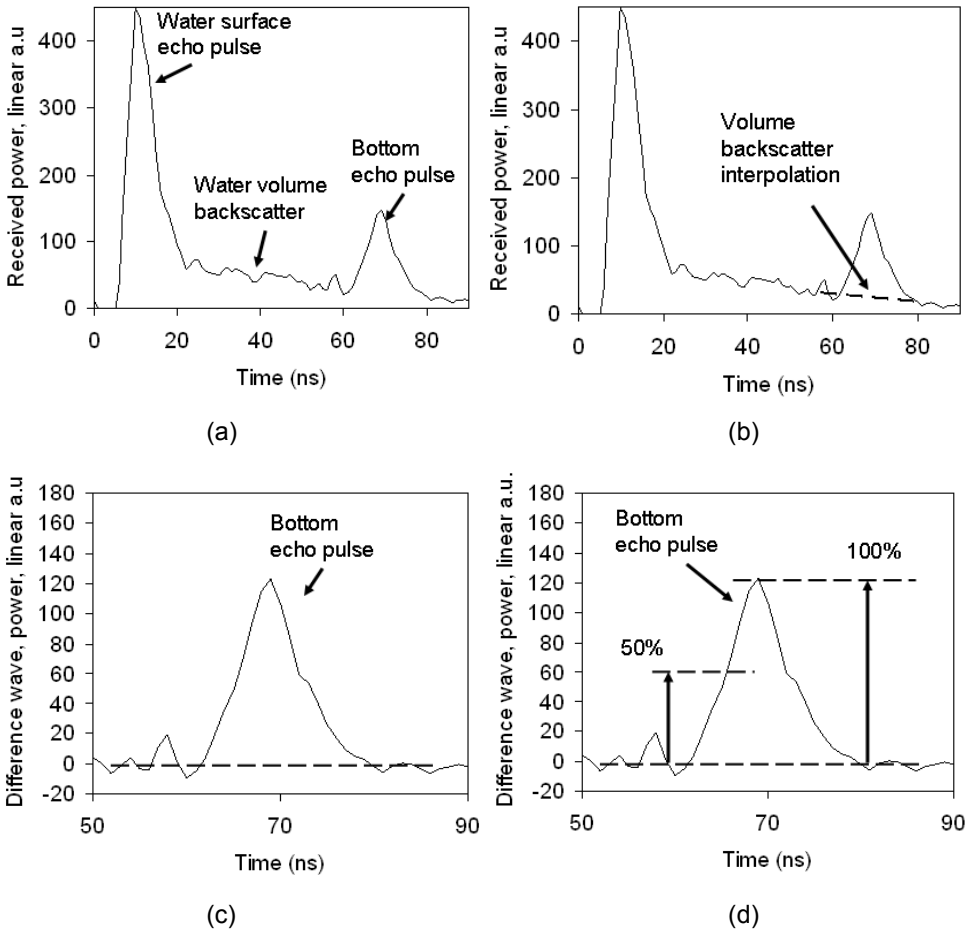

Fig. 3. Example of a lidar waveform at bottom depth 6.1 m. Parts of the waveform (a), interpolated volume backscatter (b), difference wave of the bottom echo pulse (c), and an example of 50 % and 100 % level of the bottom echo pulse (d).

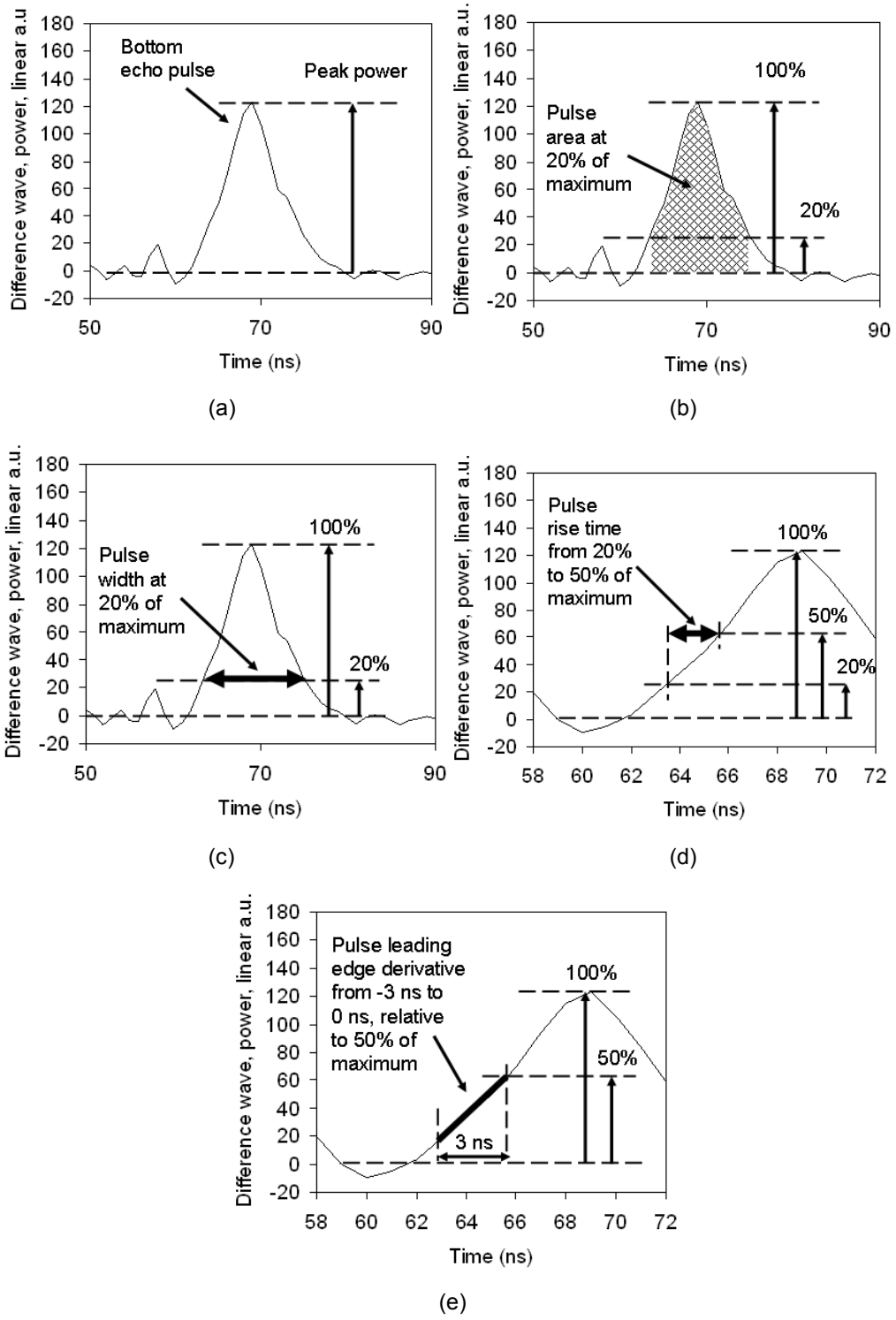

Fig. 4. Examples of bottom echo waveform features extracted from the difference wave.

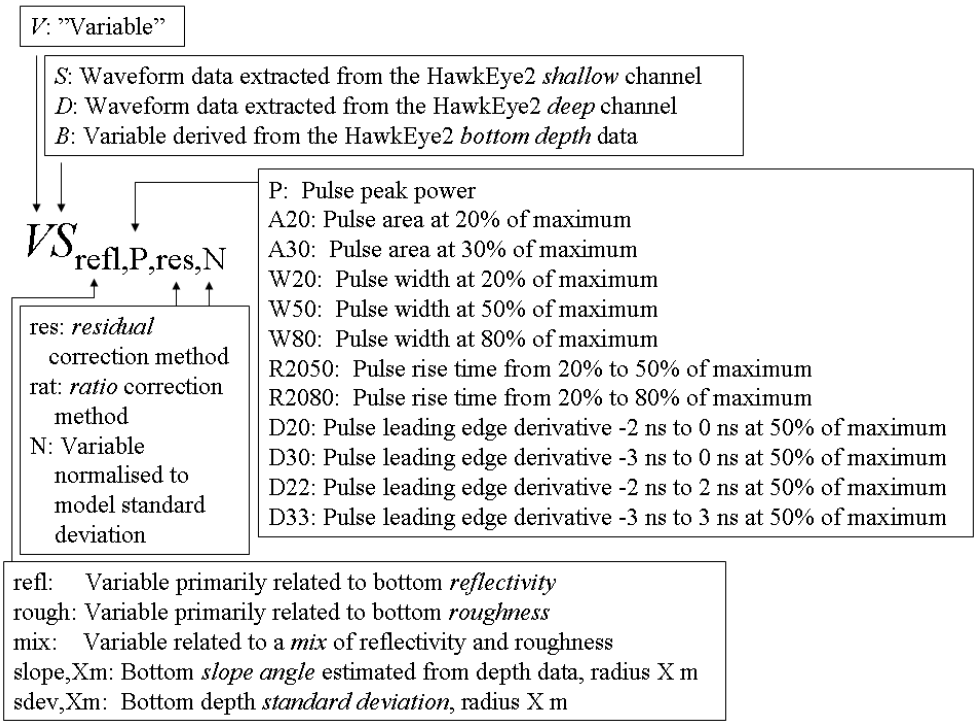

Fig. 5. Notation for the corrected classification variables from laser data.

5 Evaluation of Separability

We have used the field data together with the lidar data for a preliminary evaluation of the possibility to separate the different substrates and species using the corrected classification variables described in Section 4. In this section we examine the different classification variables and chose a preliminary set of variables based on classification tests. In Subsection 5.1 we visualise examples of classification variables for the different patches. In Subsection 5.3 different combinations of classification variables are evaluated using a multivariate classification method described in Subsection 5.2. In Subsection 5.4 we present and discuss the results for the best combination of variables.

The classification variables and corresponding correction models were evaluated using a number of different measures of accuracy:[13]

- Overall accuracy: The percentage of records of all bottom types that were classified correctly by the model.
- Producer's accuracy: The percentage of records of a certain bottom type that was classified correctly by the model. Producer's accuracy for a certain bottom type should be maximised if it is important that all records of the type are shown in the map.
- User's accuracy: The percentage classifications to a certain bottom type that was correct, i.e. showing the probability that a record classified to a bottom type actually represents that bottom type in the field.
- Confusion matrix of observed versus classified bottom types: The confusion matrix give a detailed picture of which bottom type classes are most difficult to separate from each other and where most misclassifications occur.

We performed both internal and external evaluation. For the internal validation, the model was built using all records of a certain bottom type and tested on the same records. This evaluation shows the degree of overlap between bottom types in the laser parameters (causing misclassification error). However, the internal validation gives little information of the predictive power of the model, i.e. how well it can be used to predict bottom type outside the field recordings. This was instead evaluated with external validation, where the model was built on the records from one or two patches of a certain bottom type and validated on records from another patch of the same bottom type.

5.1 Single Variable Examples

In Fig. 6 - Fig. 10 we show examples of corrected classification variables for the species and substrates taken from lidar data within a radius of 3 m from the centre of each field data patch listed in Table 1. For each field patch the number of lidar soundings is shown within parenthesis. Only the classification variables having valid values are taken into account. The valid variable ranges are checked both at the extraction stage of the waveform feature and at the correction of the feature into a classification variable. For example, a non-valid *pulse width* value can occur when the bottom echo peak power is low in relation to the waveform noise, see Fig. 3 (c). Another example is when an estimation of the bottom slope angle is missing, and thus a correction of the classification variable is not possible (the bottom slope angle is used for correction of the waveform features, see Appendix A).

Examples of variables related to bottom *reflectivity* from the *shallow* and *deep* receiver channels are shown in Fig. 6 and Fig. 7 respectively. In general, the loss (of non-valid) sounding values is larger for the shallow channel due to the lower signal level in the shallow channel (see Appendix A). We can also note the slightly larger variation (standard deviation) in the variables from the shallow channel in Fig. 6 compared to the values from

the deep channel in Fig. 7. Both the shallow and deep channel data can give uncertain values close the maximum depth limit of the lidar survey which is illustrated by the field patches ID2, ID6, and ID7, where the reflectivity values between these patches have quite large differences although taken from similar bottom type (mud). The bottom depth at these patches are about 10.5 m (Fig. 2) which is close, or on the limit of the maximum lidar depth range (11 m -12 m) at this survey. Accurate extraction and correction of variables close to the maximum lidar depth range is difficult because of the low signal-to-noise ratio at these depths. The corrections (Appendix A) for large bottom depths may need further attention. In this report we will only comment on this and make our preliminary analysis on data from shallower depths.

Examples of variable results related to the bottom *roughness* from the deep receiver channel are shown in Fig. 8 (roughness variable $VD_{rough,W20,res,N}$). Despite the large standard deviations of data within each patch, we note slightly higher average values from patches with attached macro vegetation (e.g. *Zostera marina* ID910, ID911 and *Potamogeton perfoliatus* ID38, ID40, ID42) than for patches from bare bottom partly covered with detritus (e.g. ID22, ID24, ID922). Note however the contradictory result from *Potamogeton perfoliatus* ID39, where the average is considerably lower than for the other patches with similar vegetation (ID38, ID40, ID42). This could be due to a positioning error between the lidar and field data, resulting in that the lidar data is taken from the edge or outside the monitored field patch. However, it can also reflect a real variability in the roughness signal from vegetation.

Examples of variables calculated directly from the depth data are shown in Fig. 9 (bottom slope angle $VB_{slope,3m}$) and Fig. 10 (bottom depth standard deviation $VB_{sdev,3m}$). We use them in combination with other variables for sea floor classification. In addition, we use the variable $VB_{slope,3m}$ for correction of the extracted waveform features (see Appendix A). The variable $VB_{sdev,3m}$ is the standard deviation of bottom depths within 3 m radius from the patch centre (see Appendix A). It may also be considered as a variable describing the *roughness* of the bottom, but on a slightly larger scale compared to the roughness-variables extracted from the waveform data. The variables extracted from waveform data can include information from objects, on a slightly smaller scale, *within* the laser beam footprint which has a diameter of about 3 m -5 m at shallow depths (Appendix A and Ref. [9]). Another difference between waveform variables and variables derived from bottom depth data is that the latter depend on the method used in the bottom depth extractor. Often the 50%-level of the leading edge is used for bottom depth extraction. Small objects have been shown be more easily detected at lower levels, e.g. at 20 %, of the bottom pulse peak power.[14] In Fig. 10 we note that ID39 (*Potamogeton perfoliatus* vegetation) has a relatively high depth standard deviation (roughness) compared to ID38, ID40 and ID42 with a similar vegetation. This can be compared to the waveform-derived roughness variable ($VD_{rough,W20,res,N}$) that was lower for ID39 compared to ID38, 40 and ID42. This indicates that for patch ID39, the roughness is better captured by the standard deviation of depth ($VB_{sdev,3m}$) than by the waveform-derived variable. This points out that a combination of several variables may be useful for classification of bottom features.

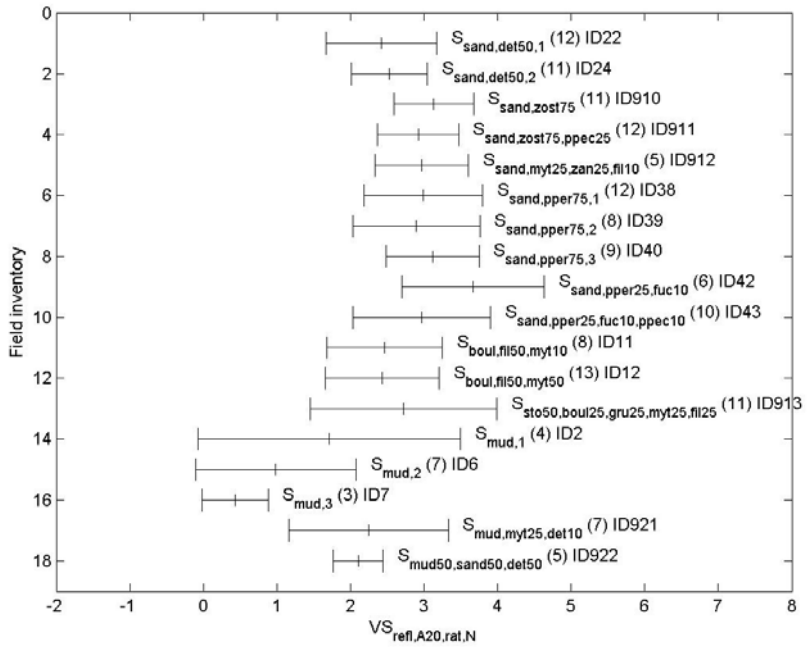

Fig. 6. Mean and standard deviation of the *shallow* channel *bottom pulse area at 20 % of maximum* (ratio-corrected, normalised) $VD_{refl,A20,rat,N}$ (according to Appendix A) for the field patches described in Table 1. For each patch the number of lidar soundings is shown within parenthesis.

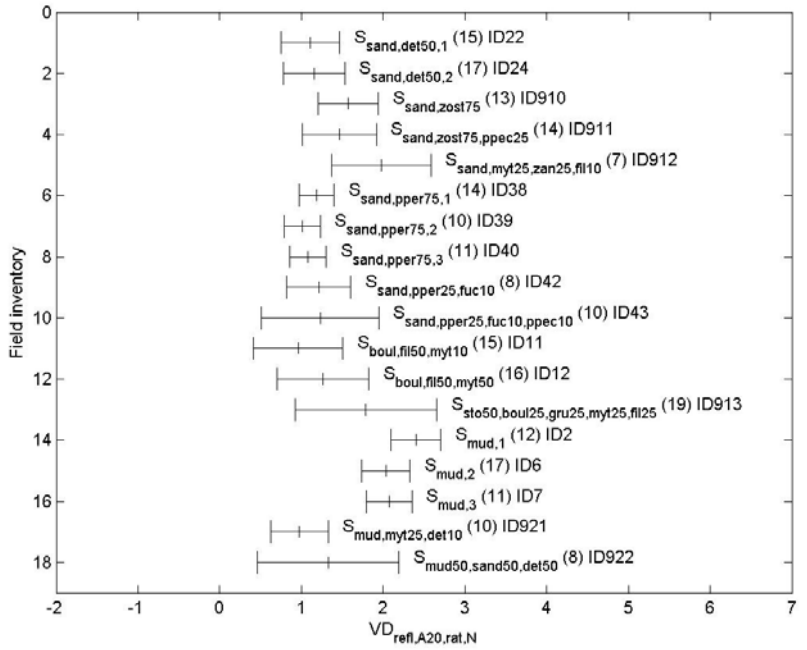

Fig. 7. Mean and standard deviation of the *deep* channel *bottom pulse area at 20 % of maximum* (ratio-corrected, normalised) $VS_{refl,A20,rat,N}$ (according to Appendix A) for the field patches described in Table 1. For each patch the number of lidar soundings is shown within parenthesis.

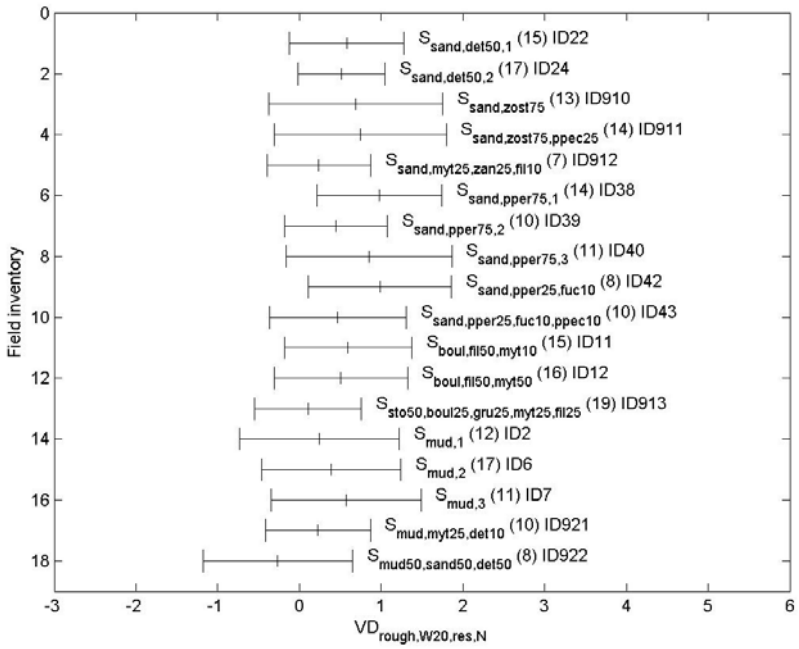

Fig. 8. Mean and standard deviation of the *deep* channel *bottom pulse width at 20 % of maximum* (residual-corrected, normalised) $VD_{rough,W20,res,N}$ (according to Appendix A) for the field patches described in Table 1.

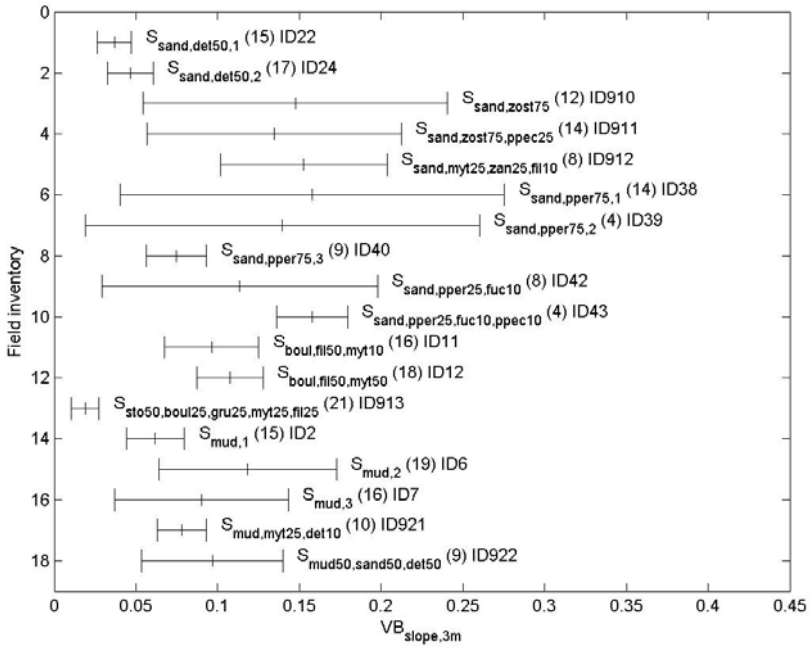

Fig. 9. Mean and standard deviation of *bottom slope angle* (in radians) $VB_{slope,3m}$ (estimated according to Appendix A) for the field patches described in Table 1. For each patch the number of lidar soundings is shown within parenthesis.

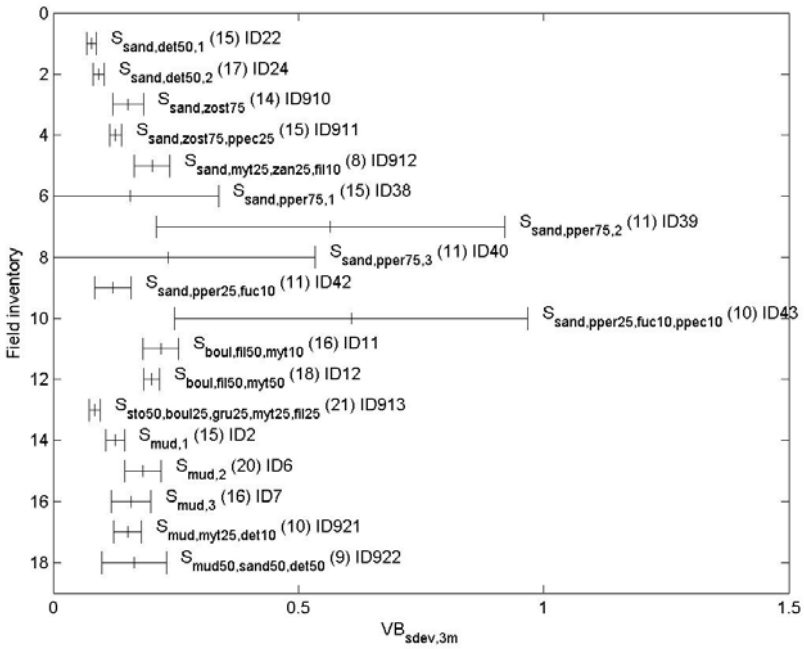

Fig. 10. Mean and standard deviation of *bottom slope standard deviation* (metres) $VB_{sdev,3m}$ (estimated according to Appendix A) for the field patches described in Table 1. For each patch the number of lidar soundings is shown within parenthesis.

5.2 Multivariate Classification Method

We have made separability tests using a multivariate classification method, where *class models* for selected species and substrates are created with training data and evaluated with evaluation data. We define the *class model* for a substrate or species class *i* from a training data set with its mean vector

$$\boldsymbol{\mu}_i = \begin{bmatrix} \mu_1 \\ \mu_2 \\ \dots \\ u_m \end{bmatrix} \tag{1}$$

and its covariance matrix

$$\boldsymbol{\Sigma}_i = \begin{bmatrix} \sigma_{11}^2 & \sigma_{12}^2 & . & . \\ \sigma_{21}^2 & \sigma_{22}^2 & . & . \\ . & . & . & . \\ . & . & . & \sigma_{mm}^2 \end{bmatrix}, \tag{2}$$

where $\mu_1, \mu_2, ..., \mu_m$ are the means each of the classification variables in the training data set. The diagonal elements of $\mathbf{\Sigma}_i$ contain the variances for each variable while the off-diagonal elements contain the covariances between variables.

For a set of *m* variables **V** the probability P_i that the lidar sounding belongs to class *i* is calculated with

$$P_i = \frac{M(\mathbf{V}, \boldsymbol{\mu}_i, \mathbf{\Sigma}_i)}{M(\boldsymbol{\mu}_i, \boldsymbol{\mu}_i, \mathbf{\Sigma}_i)}. \quad (3)$$

where *M* is a multivariate normal distribution function with

$$M = M(\mathbf{V}, \boldsymbol{\mu}_i, \mathbf{\Sigma}_i) = \frac{\exp\left[-(\mathbf{V}-\boldsymbol{\mu}_i)\mathbf{\Sigma}_i^{-1}(\mathbf{V}-\boldsymbol{\mu}_i)'/2\right]}{\left|\mathbf{\Sigma}_i\right|^{1/2}\frac{1}{\sqrt{(2\pi)^m}}}. \quad (4)$$

The classification of a lidar sounding from the *evaluation data set* (Table 1) is made by calculating probabilities for all classes P_1, P_2, ..., P_n , and choosing the class *i* with maximum probability P_i .

For the internal validation, the model was trained using all records of a certain class and evaluated on the same records. For the external validation two different sets for each class was arranged, where one was used for training and the other for evaluation. In our separability analysis we have used the four classes *Sand*, *High Vegetation*, *Low Vegetation*, and *Boulders* listed in the right part of Table 1.

5.3 Evaluation of all Variables

In order to evaluate which combinations of the classification variables that could best separate between the bottom types, we tested the separability using a large number of combinations of two or three variables with multivariate classification. The total accuracy using both internal and external validation was used to compare models including different combinations of variables. These tests revealed that:

- Using the deep channel variables in general gave better results (higher total accuracy) than using variables from the shallow channel.
- The reflectivity variable $VD_{refl,A30}$ gave better results than $VD_{refl,A20}$ and $VD_{refl,P}$.
- The roughness variables $VD_{rough,R2050}$ gave slightly better results than $VD_{rough,W20}$. This is reasonable because the shallowest part in the laser beam footprint mainly affects the leading edge of the bottom echo pulse.
- The roughness variable $VD_{rough,W20}$ gave slightly better results than $VD_{rough,W50}$ and significantly better results than $VD_{rough,W80}$. This result is consistent with our earlier results[14] where we experienced that small objects are more easily detected by pulse width measurements on a low level (e.g. 20%) than on the 50%-level of the pulse maximum height.
- The roughness variable $VD_{rough,R2050}$ gave slightly better results than $VD_{rough,R2080}$.

- The ratio-corrected and residual-corrected variables gave almost similar results for the roughness variables. The residual-corrected variable was used in the following analysis because it has a physical explanation for *roughness* in that the unit of the residual is nanoseconds which can be transformed to height (e.g. for vegetation above the bottom), see Appendix A.
- Including the bottom slope angle $VB_{slope,3m}$ in the classification gave better results than if it was not included.
- Un-normalised variables gave slightly better results than normalised variables. E.g. $VD_{rough,R2080,res}$ gave better slightly better result than $VD_{rough,R2080,res,N}$. In the following analysis we however used the normalised variables because these have a larger potential to work for data sets with large variations in depth.
- The ratio-corrected reflectivity variables gave slightly better results for the *reflectivity* variables than the residual-corrected. The ratio-corrected variable was used in the following analysis also because it has a potential for calculation of calibrated reflectance of bottom substrates (Appendix A).
- The leading edge derivative variables (e.g $VD_{mix,D30,res}$) give almost similar results as the rise time variables (e.g. $VD_{rough,R2080,res}$). In the following analysis we use the rise time variable $VD_{rough,R2080,res}$. It should however be noted that the leading edge derivative variables may give higher sensitivity for weak pulses when the 50% level is more clearly defined than the 20% level. On the other hand, the leading edge derivative variables may be less sensitive for strong echoes with extended leading edges because the start point of the pulse may occur >3 ns before the 50%-level of the bottom echo.

5.4 Separability Analysis with the Best Variables

Based on the results from the initial evaluation of classification variables described in Subsection 5.3 we identified $VD_{refl,A30,rat,N}$ and $VD_{rough,R2050,res,N}$ as the best variables for reflectivity and roughness, respectively. Bottom slope $VB_{slope,3m}$ and bottom depth standard deviation $VB_{slope,3m}$ were also identified as important contributors to the classification. In the following analysis we used a combination of these four variables in order to explore to what extent the different bottom types can be separated using these variables and which types are more difficult to separate. It should be noted that other variables and combinations of variables may be useful depending on the specific conditions in the survey data. It may also be of benefit to include more variables than four. For example, the shallow channel data could be used as it is a separate and independent measurement from the deep channel. Although the shallow channel data exhibits more noise than the data from the deep channel, shallow data may be useful e.g. at shallow depths. Due to the limited amount of field data patches, we have however restricted the following analysis to a maximum of four variables of which two are derived from waveform data.

The model including only reflectivity and roughness had a low overall accuracy, only around 50% in both internal and external validation (Table 2). Comparison of accuracy for the different bottom types shows that producer's accuracy (PA) was low for all types (Table 4). The model was slightly better in classifying sand and boulders compared to the other types, but the accuracy was still <60 % in the external evaluation for these types. The low accuracy is not surprising given that the variation in reflectivity and roughness was large for many bottom types (Fig. 6 - Fig. 8).

Including the slope and depth standard deviation in the model improved the overall accuracy both according to internal and external validation (Table 3). The external validation indicates that the depth standard deviation contributed more to improve the model, but the best overall accuracy was achieved with the model including all four variables (70.9 % accuracy in external validation). This illustrates that when combined with depth-derived variables (in this case slope and depth standard deviation), the

waveform variables has the potential to substantially improve classification accuracy of substrates and vegetation.

Comparison of accuracy for the different bottom types shows that the depth standard deviation mainly improved the PA for low vegetation, high vegetation and boulders. As discussed in Subsection 5.1, this variable reflects topographic roughness at a slightly larger scale than the waveform derived roughness and can be expected to differ with height of vegetation and between a smooth sand surface and a boulder field. Including slope mainly improved the PA for boulders and low vegetation. In the present study, the slope was higher in the boulder patches compared to patches with sand (Fig. 9). This may be a common pattern, since boulders often dominate in areas with steeper slopes where the accumulation of fine sediment is low. However, the difference in slope between sand and boulders was rather small and patches with sand and vegetation had in many cases a higher slope than the boulder patches. This shows that in the present study the difference in slope may be driven as much by the fact that patches of a certain vegetation type are often close in space as by general differences between bottom types. The importance of slope should therefore be further evaluated using a larger set of field data.

The best model, including both the slope and the depth standard deviation, showed a high producer's accuracy for all bottom types except sand (Table 4). The confusion matrix shows that sand is often erroneously classified as high vegetation by the model. The prediction of sand is conservative, less than half of the sand records are classified correctly but all records classified as sand are correct (100% user's accuracy). The misclassification of sand to high vegetation when the depth standard deviation was included can be attributed to the large variation in this variable for high vegetation, while the variation for sand is very small (Fig. 10). This example illustrates how a difference in variation between bottom types can affect producer's and user's accuracy in different directions.

Table 2. Total accuracy (TA) in internal and external validation of models including different combinations of the laser variables $VD_{refl,A30,ratN}$ (Refl), $VD_{rough,R2050,resN}$ (Rough),.bottom slope (Slope) and Bottom depth std dev (Stdev). The number of data points used to validate the model (n) differs because data for some of the variables were missing from a few data points.

	Intern. Eval		Extern. Eval	
	TA (%)	**n**	**TA (%)**	**n**
Refl Rough	50.9	114	50.0	58
Refl Rough Slope	71.4	105	54.5	55
Refl Rough Stdev	73.7	114	65.5	58
Refl Rough Slope Stdev	87.6	105	70.9	55
Slope	48.2	110	34.5	58
Stdev	49.6	121	34.4	61
Slope Stdev	78.2	110	51.7	58

Table 3. Producer's accuracy (PA) and User's accuracy (UA) for the four bottom types with models including different combinations of the laser variables $VD_{refl,A30,ratN}$ (Refl), $VD_{rough,R2050,resN}$ (Rough),.bottom slope (Slope) and Bottom depth std dev (Stdev).

		Sand	LowVeg	HighVeg	Boulders
Refl Rough	PA	52.9	50.0	36.4	56.3
	UA	52.9	46.7	50.0	50.0
Refl Rough Slope	PA	41.2	61.5	44.4	68.8
	UA	100.0	50.0	40.0	50.0
Refl Rough Stdev	PA	41.2	64.3	90.9	75.0
	UA	100.0	64.3	40.0	100.0
Refl Rough Slope Stdev	PA	41.2	92.3	88.9	75.0
	UA	100.0	63.2	47.1	100.0
Slope	PA	47.1	0.0	44.4	44.4
	UA	88.9	0.0	13.8	44.4
Stdev	PA	23.5	26.7	90.9	16.7
	UA	80.0	100.0	20.4	100.0
Slope Stdev	PA	11.8	64.3	88.9	61.1
	UA	66.7	56.3	28.6	100.0

Table 4. Confusion matrices of the models including the laser variables $VD_{refl,A30,ratN}$ (Refl), $VD_{rough,R2050,resN}$ (Rough) (A) and all four variables (B) for the external validation data, including producer's accuracy (PA) and user's accuracy (UA).

A. Refl Rough

Obs\Class	Sand	LowVeg	HighVeg	Boulders	**Total**	**PA (%)**
Sand	9	3	0	5	17	**52.9**
LowVeg	1	7	3	3	14	**50.0**
HighVeg	5	1	4	1	11	**36.4**
Boulders	2	4	1	9	16	**56.3**
Total	17	15	8	18	58	
UA (%)	**52.9**	**46.7**	**50.0**	**50.0**		**50.0**

B. Refl Rough Slope Stdev

Obs\Class	Sand	LowVeg	HighVeg	Boulders	**Total**	**PA (%)**
Sand	7	2	8	0	17	**41.2**
LowVeg	0	12	1	0	13	**92.3**
HighVeg	0	1	8	0	9	**88.9**
Boulders	0	4	0	12	16	**75.0**
Total	7	19	17	12	55	
UA (%)	**100.0**	**63.2**	**47.1**	**100.0**		**70.9**

6 Conclusions

We have studied the possibilities to separate different bottom substrates and vegetation using variables derived from airborne lidar data. The variables were either derived from depth data (bottom slope and depth standard deviation), or extracted from the lidar waveform.

The extracted waveform variables can be related to the bottom substrate or vegetation reflectance, roughness, or a mix of both. Correction models for the extracted waveform features were applied producing a set of classification variables. The corrections models include corrections for e.g. water turbidity, bottom depth, and the flight altitude.

The evaluation of separability between different substrates and vegetation was performed with laser data taken from patches identified by interpreted underwater video data.

We studied the classification variables as single variables and performed separability tests using a multivariate classification method. Based on evaluation of a large number of waveform-derived classification variables we chose a preliminary set of four variables. With the preliminary set of variables we obtained a total classification accuracy of about 70% between the four bottom types Sand, Low Vegetation, High Vegetation and Boulders. This illustrates that when combined with depth-derived variables (in this case slope and depth standard deviation), the waveform variables have the potential to substantially improve classification accuracy of substrates and vegetation.

Waveform classification variables from the Hawk Eye II shallow and deep receiver channels were evaluated. We have noted better classification results (higher total accuracy) with variables extracted from the deep channel compared to variables from the shallow channel. The larger misclassification for the shallow channel variables may be caused by lower signal-to-noise ratio for bottom echoes in the shallow channel waveform. Both the shallow and deep channel waveform variables gave uncertain values close the maximum depth limit of the lidar survey (11 m -12 m). Accurate extraction and correction of variables close to the maximum lidar depth range is difficult because of the low signal-to-noise ratio at these depths and the variable corrections for large bottom depths may need further development than obtained in this report.

We found that a combination of several variables can be appropriate for separation of different bottom types and vegetation. For example, the bottom roughness can be captured either by a waveform variable such as the bottom echo pulse rise time, or the standard deviation of depths in the vicinity of a lidar sounding. These two variables both indicate roughness but on slightly different scales.

Appendix A. Correction Models for Laser Waveform Variables

A1 Introduction

The following correction scheme concerns lidar data from the HawkEye II – Airborne coastal survey system, by Airborne Hydrography AB (AHAB), Sweden (http://www.airbornehydro.com). The Hawk Eye II system surveys both land and sea floor simultaneously. Our work concerns the *bathymetric* data from the system. The system uses a pulsed, infrared (1064 nm) and green (532 nm) laser for the bathymetric sounding. The infrared pulses are reflected at the water surface whereas the green pulses proceed into the water volume. The laser light backscattered from the sea surface, the water volume and the sea floor is collected in multiple, high-sensitivity receivers. Hawk Eye II produces measurements in photoelectrons at the photocathode of each returned laser pulse in 1-ns time bins. When shown as a time series, the collection of all measurements for a single pulse is called a waveform. The received laser light is divided into two separate channels using a beam splitter. The first is a *shallow*-water channel which receives about 30 % of the light, and the second a *deep*-water channel which receives about 70 % of the light. The shallow and deep channels have FOV:s of approximately 25 mrad and 50 mrad respectively. The deep channel allows for more efficient collection of photons backscattered from larger depths. The shallow and deep channels each have a quad-pixel detector. Thus, from one single emitted laser pulse, four waveforms are received in both the shallow and deep channels.

The received waveforms are digitized for further processing and the depth is determined by the time lapse between surface and the bottom echoes. The integrated differential GPS enables positioning of surface, sea floor, and objects in the water column in 3 dimensions in WGS 84 coordinates. The Hawk Eye II system is equipped with a two axis, servo-controlled, scanner mirror to space the sounding spots evenly on the surface. The nominal system optical axis incidence angle from the vertical is 15°-20°.

The Hawk Eye II system simultaneously collects 4000 bathymetric lidar soundings per second. The sounding spot density for bathymetric data is programmable from 0.5 m x 0.5 m to 3 m x 3 m depending on survey requirements. The flight altitude is approximately between 200 m and 500 m. The swath width of the system is typically 0.2-0.6 times the altitude and the aircraft speed typically 120-180 knots. The Hawk Eye II high laser sounding frequency and the programmable spot density allows high area coverage combined with accurate survey data collection. The system compensations for flight deviations allow for minimized overlap between adjacent flight lines. The Hawk Eye II system Operator Console software includes an extensive range of tools such as: coverage plots, real time 3-D views of the surveyed area, flight line plan, background map, system parameters, laser pulse responses, and depth ranges. Many attributes are stored for each sounding as a basis for further analysis, post processing, and quality control. The data is stored on hard disks transported from the aircraft for further post processing. In brief, the post processing consists of:

- Refinement of position data with use of navigation post processing software and data from reference stations.
- Analysis of Hydrographic and Topographic elevation data by the AHAB Coastal Survey Studio (CSS) software. The CSS tool includes several advanced algorithms for sub-surface objects detection and identification, quality checks of data, estimates of water and sea floor parameters and decision support to the data cleaning process and interfaces to third party software.

- A cleaning process which includes quality check of the data and removal of faulty data points.
- Further post processing by third party commercially available software or the Coastal Survey Studio depending on the end user requirements for visualization.

In our additional post-processing we explore further use of the time-resolved lidar waveform. Specifically, our purpose is to extract features from the waveform and to correct these into variables that can be used for studying the possibility of classification of the sea floor.

A2 The Lidar System Parameters

A schematic illustration of the lidar system is shown in Fig. 11. The water depth D is calculated from the time interval between the surface echo and the bottom echo, and each sounding is appropriately corrected for wave height. For a more detailed presentation of how depth estimations are made from the sensor signals we refer to Refs. [15-17]. The significant system parameters are the green laser output pulse energy E_0, the FWHM laser pulse length t_0, laser beam divergence B_σ (defined as the full angle between the two points on a Gaussian irradiance distribution that are $e^{-1/2} = 0.607$ times the maximum value), flight altitude H, system optical efficiency η, and incident beam off-nadir angle θ_0. The distance in air between the lidar and the water surface along the optical axis is referred to as the *slant range* $H/\cos(\theta_0)$. The receiver parameters are the one-dimensional field of view (FOV) and the receiver aperture area A_R. For a flat water surface, the off-nadir angle in water is $\theta_w = \arcsin\{\sin(\theta_0)/n_w\}$, where $n_w = c_0/c_w$, and c_0 and c_w are the velocities of light in air and water, respectively. The lidar system and environmental parameters are summarized in Table 5. The typical parameter values shown in Table 5 are used in the following simulations unless otherwise is stated.

Table 5. Lidar System and Environmental Parameters

Parameter	Value range	Typical value	Unit
Pulse energy (λ = 532 nm) (E_0)		3	mJ
Beam off-nadir angle (θ_0)	15-20	20	°
Flight altitude (H)	200-500	200	m
Beam divergence, full angle at the $e^{-1/2}$ -level of maximum from a Gaussian distribution (B_σ)	8-12	10	mrad
Pulse length (FWHM) (t_0)		3	ns
Optical system efficiency (η)			
Aperture area (A_R)		0.025	m^2
Field of view, full angle (FOV)		25 (shallow) 50 (deep)	mrad
Two-way atmospheric loss (T_{atm}^2)		0.9	
Bottom depth (D)			m
Bottom reflectivity (ρ_{532})			
Bottom slope angle		0 (flat, horizontal bottom)	°

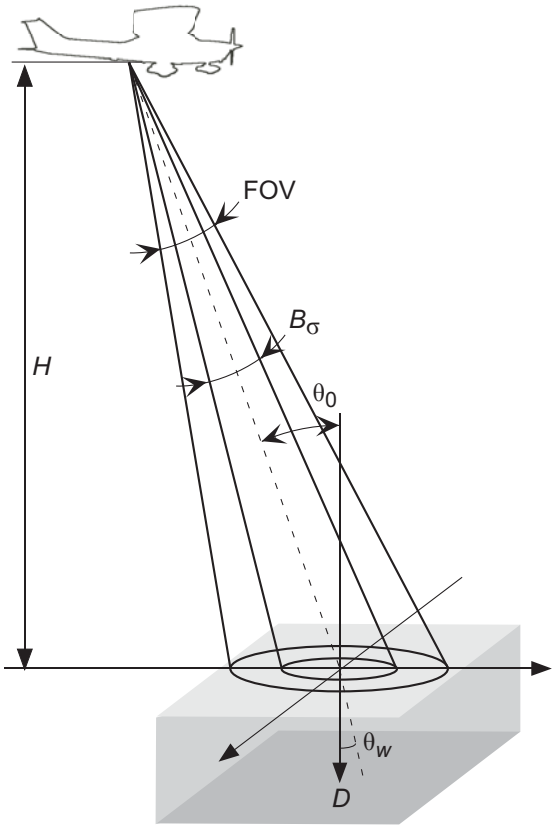

Fig. 11. Schematic illustration of the depth sounding lidar system.

A3 The Waveform

Sea floor classification algorithms can use characteristics from the received lidar waveform and other information obtained from the lidar data such as the bottom slope angle. Basic processing of the waveform includes linearization of the received and digitised waveform. In the Hawk Eye II system, the measured waveforms pass through the system: Detector - Amplifier - Digitiser. Before further processing, we convert the measured waveforms to linear scale using instantaneous amplifier gain values accessible from the survey data disk. The linearization is made for each individual sounding. In the linearized waveform we can measure the received power at an instant in a waveform and relate this value, on the same scale, to other values in the same waveform. With a linearized waveform, we can compare measured values with those generated from simple lidar equations or more advanced simulation models. The lidar equations and simulation models are used for development of accurate corrections of waveform data which will be outlined in the following sections. It should be noted that the linearization is not 100 % exact as the gain values used for linearization is a model of the actual gain.

An example of a linearized waveform from the HawkEye II system is shown in Fig. 3 (a). The main signals in the waveform are the water surface echo, the water volume backscatter, and the bottom echo pulse. In addition, the waveform contains noise which is a combined effect from environmental background light and noise generated in the optical detector and receiver electronics. In our following extraction of sea bottom characteristics from the waveform, we calculate the waveform characteristics of the bottom echo pulse from the *difference wave* (Fig. 3 (b)-(c)). The difference wave is calculated as the difference between the waveform, in linear scale, and an interpolated volume backscatter wave under the bottom echo pulse.[9, 10] The basic principle for estimation of the bottom depth is by measuring the time lapse between the surface echo and the 50% level on the leading edge of the bottom echo, see Fig. 3 (d).

A4 Features Extracted from the Lidar Waveform

We aim at the extraction of two fundamental characteristics of the sea bottom namely its *reflectivity* (at wavelength 532 nm) and its *roughness.* An example of a waveform feature that can be used for sea floor roughness estimation is the width of the bottom echo pulse. From earlier experiments[8, 11] and simulations [10, 12] we have experienced that small objects on the sea bottom can be detected by an increase in the reflected bottom pulse width. The bottom pulse width can also be used for indication of elevated vegetation on the sea floor. Another example of a waveform feature is the peak power of the bottom echo which can be can be used to estimate the sea floor reflectance. The estimation of reflectance involves corrections of the bottom pulse peak power in the waveform for several influencing factors such as the water turbidity, water depth, and flight altitude. The correction process is sometimes referred to as an *inversion* of the lidar equation.[4] The *lidar equation* can actually contain several equations depending on its complexity for description of different phenomena in the waveform related to lidar system and environmental parameters.

Reflectivity and *roughness* parameters can be extracted from the bottom echo pulse in many different ways. We have defined a basic set of such parameters and corresponding correction schemes for further use in classification studies. In Fig. 4 we show schematic descriptions of a basic set of bottom echo features. In Fig. 5 a description of classification variables and corresponding notation for the corrected variables is given. The features are extracted from the bottom echo difference wave. A necessary step is to correct these features to *classification variables* that can be used for classification of the sea floor. Using simulated waveform data, we will make correction models for each of the waveform features. The correction models include effects from e.g. the water turbidity, the bottom depth and the flight altitude. The purpose of the correction models is to remove effects from the lidar system and water volume to obtain pulse data which mainly are influenced by the bottom type or vegetation.

A5 Estimation of Bottom Slopes and Depth Standard Deviation

We use the depth data for estimation of bottom slope angle and bottom depth standard deviation within small regions around each sounding position. Two different sizes of regions are used; a radius of 2 m and 3 m around each sounding, respectively. For estimation of bottom slope angle, a plane is fitted to a collection of lidar soundings in a least squares sense. In tested data set, the depth data consists of a randomly spaced point cloud with average point density of approximately 0.8 soundings per m^2. At positions where flight lines are overlapping the point density is higher and at positions where e.g. the depth is close to the maximum lidar bottom range the point density is lower. For calculation of both bottom slope angle and bottom depth standard deviation, a minimum number of three soundings is required, we otherwise mark the values as non-existing.

Both the bottom slope angle and bottom depth standard deviation can be used as inputs for bottom classification algorithms. In addition we will, in the following sections, use the estimated bottom plane as input for the correction of variables extracted from the lidar waveform. For the corrections, we will use the cosine of the angle between bottom downward normal $\hat{\mathbf{n}}_b$ and the in-water lidar optical axis unit vector $\hat{\mathbf{n}}_l$, calculated as the dot product $\hat{\mathbf{n}}_b \cdot \hat{\mathbf{n}}_l$ between the unit ray vectors, see Fig. 12.

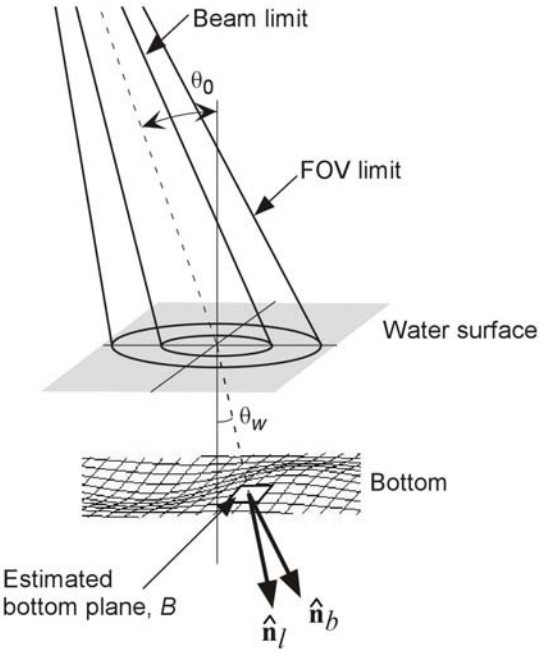

Fig. 12. Illustration of the estimated bottom plane *B*, its normal $\hat{\mathbf{n}}_b$ and the in-water lidar unit vector $\hat{\mathbf{n}}_l$.

A6 Estimation of Water Optical Turbidity

Our correction methods use an estimate of the local water turbidity around each specific sounding position. The turbidity is quantified as the lidar attenuation coefficient K_{lidar}.[9] The lidar attenuation coefficient is estimated from the decay in the volume backscatter curve (see Fig. 3 (a)). The decay is measured in the interval from 3 m to 5 m depth below the sea surface. The shallow limit at 3 m is used to avoid interference from the water surface echo pulse. The deeper depth limit conveys that turbidity estimates from the volume backscatter curve only can be made at bottom depths larger than 5 m. In our implementation we have applied a minimum depth requirement of 6 m for estimation of K_{lidar} to avoid interference from the bottom echo.

In addition to water turbidity, the K_{lidar} parameter also includes effects from the lidar system FOV. The FOV-effect on K_{lidar} is caused by the reduction of backscattered power due to a limited FOV.[9] Thus, for our correction methods, two separate estimates of K_{lidar} are calculated for the shallow and deep receiver channels respectively. The K_{lidar} estimates form each individual sounding contain noise which can be related to the noise in the backscatter signal (see Fig. 3 (a)). Therefore, we apply a smoothed average of the K_{lidar} -estimates averaged from adjacent soundings within a 15 m radius from each individual sounding.

To handle the survey areas with missing K_{lidar} estimates, shallower bottom depth than 6m, we have used a nearest neighbour algorithm in two steps. In the first step a missing K_{lidar}-value is assigned the K_{lidar}-value from the nearest sounding within 100 m radius, where only neighbours from the same flight line are used. If missing K_{lidar}-values exist after the first step, the nearest neighbour value is used regardless of distance from the actual sounding position and flight line. We have chosen this two-step scheme because it favours nearest neighbour interpolation from the same flight line because turbidity can vary between flight line data collection if the time between flight line surveys differ. One example of such a scenario would be if a large area is surveyed over several days.

A7 Simulation Model

A simple form of the lidar equation for returned bottom pulse peak power can be written

$$P_{\text{peak}} = P_0 \eta T_{\text{atm}}^2 (1-\rho_s)^2 \rho_{532} \frac{A_R \cos^2\theta_0}{(n_w H + D)^2} e^{-2K_{\text{lidar}}} F_{\text{stretch}}, \quad (5)$$

where P_0 is the transmitted pulse peak power, ρ_s the Fresnel reflection coefficient of the air-water interface, and F_{stretch} a reduction factor (between 0 and 1) of the returned peak power which is caused by propagation-induced pulse stretching and pulse stretching caused by the receiver detector and electronics. Other parameters in Eq. (5) are according to the previous sections and to Table 5. Our correction methods are based on more detailed modelling than Eq. (5). However, Eq. (5) gives a general idea of the relations between important parameters.

The model involves e.g. effects of pulse stretching and FOV-effects on both water volume backscatter and on the bottom pulse echo We have used a waveform simulation model, which is described in detail in Ref. [9] Here, we give a brief model description. The model for transfer of the optical beam through the sea surface is a two-scale model similar to the models proposed by Mobley[18] and McLean.[19] The large-scale part of the model includes a representation of the gravity waves generated on a triangular grid that resolve the gravity wave components. The light incident on a gravity wave facet is transferred and reflected according to a capillary wave model governed by Snell's law and Fresnel's formula. The transfer model for the capillary waves (function of wind speed and incidence angle) is implemented with Monte Carlo simulations as described by Mobley.[18] The lidar pulse response for propagation from the lidar transmitter to the sea floor and back to the receiver is calculated as a weighted sum of individual pulse responses for each transmitted and received beam pairs through all pairs of gravity wave surface facets. Each individual path is given a weight corresponding to the power transmitted over that path. The weighting factor for an individual water volume pulse response for a gravity wave facet pair is the product of the transmitted power through the two facets. The individual responses from the water volume backscatter are calculated with an analytic technique developed by Katsev *et al*.,[20] which allows that the source and receiver are spaced apart and their axes oriented in different directions. With this terminology we thus represent one gravity wave facet as the source and the other as the receiver. We use an in-water beam propagation model developed by McLean *et al.*[21] which accounts for both unscattered and scattered propagation. A two-step energy calibration scheme is included in our model. The method conveys that radiometrically accurate power values are obtained for comparison between the volume backscatter and the sea floor return, and also that the reduction of backscattered power due to a limited field-of-view FOV can be examined. Our noise model for the waveform noise is a shot noise model with Gaussian distribution with zero mean and standard a deviation that varies with the signal level at each instant in time within the waveform.

A8 Classification Variables and Pulse Models

In this section we present results from simulations of the lidar and environmental parameter influence on the extracted waveform features, shown in Fig. 4. Based on extracted features from the simulated waveforms, we have created a *pulse model* for each of the waveform features.

In our simulations the stochastic part of the results has its origin in several factors such as the simulated waveform noise, the effects from the wavy sea surface, and varying simulated flight directions over a sloping bottom. For simulations on sloping bottoms the lidar optical axis azimuth direction was varied in steps of 45°. That is, the angle between the lidar optical axis azimuth and the bottom slope direction was 0°, 45°, 90°, 135°, and 180°. A wind speed of 3 m/s was used for the wind driven sea surface model. For sloping bottoms, the bottom slope angle was varied between 0° and 20° from the horizontal. With a lidar air off-nadir angle θ_0=20° and a corresponding in-water off-nadir angle θ_w of about 15°, the maximum angle between the bottom normal and the lidar optical axis was approximately 35°. In the following figures (Fig. 13 - Fig. 33) we denote the depth *D* as the input depth, "true depth", to the simulation model. For sloping bottoms the depth is the vertical depth from the lidar optical axis hit on the mean water surface.

The purpose of the pulse model is to model the effects from the lidar system, geometry, bottom depth and water turbidity, and isolate those effects from the bottom reflectivity and roughness. For example, a *classification variable* can be calculated e.g. as the *residual* (in our case the difference) between the extracted waveform feature and the pulse model of the same feature under the same conditions. The pulse models have analytic expressions and some of the coefficients need to be estimated from real, measured data. The coefficients are estimated from a *training data set* of the measured lidar data. It should be noted that this training data set is not taken from field data positions, and thus does not require field data. It is rather a model representation of the whole survey including its interval of bottom depths, flight altitudes, water optical turbidity, bottom reflectance, slopes, roughness, and other system or environmental factors. The training data used, is a sparse representation of the complete data set from the survey. In our preliminary evaluation we have used each 37th sounding of a test set from a survey, which resulted in a training data set of about 70 000 soundings. The suitable reduction factor for a data set should be a balance between several factors such as the original size of the survey data set, variations in water turbidity, and available computing capacity. It should be noted that the reduction factor should be an odd number, or that the reduction of data is controlled in other ways, to avoid biases related to the different channels in the receiver.

In the following we present analytic equations for the pulse models. We have developed these models by manual inspection and fitting of analytic models to the simulated results. For each waveform feature, we apply four different corrections where the first and second are residual- and ratio- corrected variables. The third and fourth corrections are normalised versions of the two first variables. These four correction methods are generated for further evaluation of the classification variables.

As an example, for the *bottom pulse peak power* (Fig. 4 (a) and Fig. 5), we calculate the *residual*-corrected (res) classification variable with

$$VS_{\mathrm{refl,P,res}} = FS_{\mathrm{refl,P}} - M_{\mathrm{refl,P}}\,, \tag{6}$$

where FS_{refl} and $M_{\mathrm{refl,P}}$ respectively are the *extracted waveform feature (F)* and the *pulse model (M)* of the pulse peak power (subscript P) in the *shallow* channel *(S)*. In the second method we calculate the *ratio*-corrected (rat) variable with

$$VS_{\mathrm{refl,P,rat}} = \frac{FS_{\mathrm{refl,P}}}{M_{\mathrm{refl,P}}}\,. \tag{7}$$

An advantage with ratio-correction instead of residual-correction of a *reflectivity* variable is that a ratio-corrected variable has a potential for calculation of *calibrated reflectance* of the bottom. To obtain calibrated reflectance measurements of the bottom, we anticipate that either accurate lidar system calibration or data from bottom patches with known reflectance are applied. If the correction is accurately made, then the calibrated reflectance can be obtained only by one multiplication factor applied to the ratio-corrected variable.

An advantage with residual-correction instead of ratio-correction of a *roughness* variable is that the residual-corrected variable has a more physical explanation for roughness in that the unit of the residual is nanoseconds which can be transformed to height (e.g. for vegetation above the bottom).

The *normalised* residual-corrected variable is calculated with

$$VS_{\mathrm{refl,P,res,N}} = \frac{VS_{\mathrm{refl,P,res}}}{VS_{\mathrm{refl,P,res},\sigma}}, \tag{8}$$

and the *normalised* ratio-corrected variable with

$$VS_{\mathrm{refl,P,rat,N}} = \frac{VS_{\mathrm{refl,P,rat}}}{VS_{\mathrm{refl,P,rat},\sigma}}, \tag{9}$$

where $VS_{\mathrm{refl,P,res},\sigma}$ and $VS_{\mathrm{refl,P,rat},\sigma}$ are estimations of the $VS_{\mathrm{refl,P,res}}$ and $VS_{\mathrm{refl,P,rat}}$ variable standard deviation based on lidar soundings taken from a *training data set* of the measured lidar data.

The analytic pulse models are based on a large number of waveform simulations. In the remaining parts of this section we present examples of simulation results and our pulse models created for each of the bottom echo features extracted from the linearized lidar waveforms. The features are grouped according to the examples shown in Fig. 4, and thus each group is assigned a separate analytic pulse model.

Pulse Models

Due to the influence of the water surface echo on the bottom signal we have defined two main depth zones for the pulse models (separated by a depth limit D_{lim}), one zone is close to the sea surface and the other is for larger depths. In addition, the pulse model coefficients, estimated from the *training data set* of the measured lidar data, are calculated in internal depth intervals within the two zones. This method is motivated mainly for two reasons. The first reason is that we estimate the K_{lidar} from the volume backscatter at 3 m - 5 m depth, and that K_{lidar}, which attenuates the bottom echo, is actually itself a function of depth. By using different depth intervals for estimation of the coefficients, we obtain local models (in depth) where the coefficients catch the possible errors in K_{lidar} values for all depths. The second reason that the waveform linearization is not 100 % perfect over the whole depth range. Individual coefficients are estimated for each of the pixels in both the shallow and the deep channels. This is motivated by the fact that each pixel has a specific and individual FOV and also a slightly different sensitivity.

Pulse Peak Power

Simulation results for the bottom echo pulse peak power are shown in Fig. 13 - Fig. 16. We write the pulse model for the pulse peak power as

$$M_{\text{refl,P}} = C_{\text{P1}}\rho_{532}\frac{\cos^2\theta_0}{H^2}\exp(-C_{\text{P2}}K_{\text{lidar}}D)\exp\left[10\hat{\mathbf{n}}_b\cdot\hat{\mathbf{n}}_l\right]+M_{\text{P}}, \qquad (10)$$

where C_{P1} and M_{P} are estimated from a *training data set* of the measured lidar data. It should be noted that separate and different values for C_{P1} and M_{P} are estimated respectively for the shallow and deep channels. The C_{P2} coefficient is set to

$C_{\text{P2}} = 3$ for FOV 25 mrad (shallow channel), and

$C_{\text{P2}} = 2.5$ for FOV 50 mrad (deep channel)

for bottom depths $D > D_{\text{lim}}$. The depth limit D_{lim} is set to a default value of 3 m, but this value may be adjusted depending on the water turbidity and other specific conditions in a lidar survey. For bottom depths $D < D_{\text{lim}}$

$C_{\text{P2}} = 2$ is used for both FOV 25 mrad and 50 mrad.

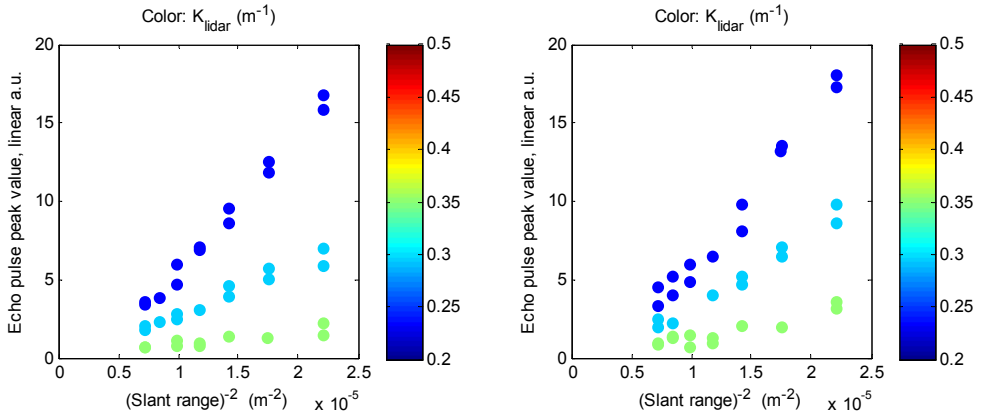

Fig. 13. Simulation results for *echo peak power* with respect to inverse squared slant range for the shallow (a) and deep (b) channels. The bottom depth is 7m and other parameters are according to typical values in Table 5.

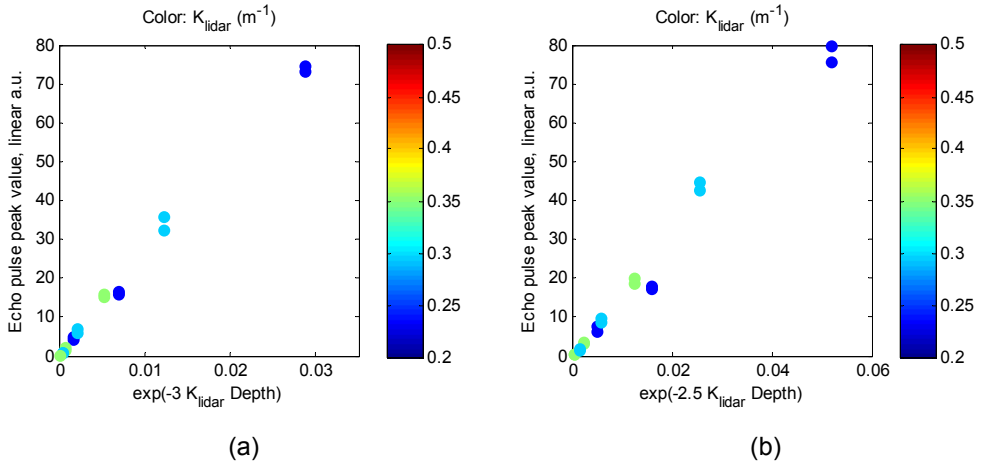

(a) (b)

Fig. 14. Simulation results for *echo peak power* with respect K_{lidar} and bottom depth for the shallow (a) and deep (b) channels. The *bottom depth range is from 5 to 12 m*. Other simulation parameters are according to typical values in Table 5.

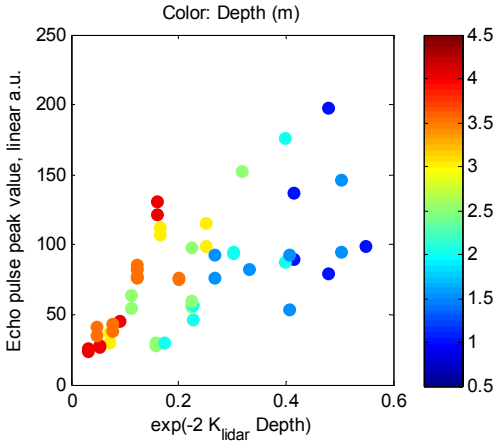

Fig. 15. Simulation results for *echo peak power* with respect K_{lidar} and bottom depth for the shallow channel. The *bottom depth range is from 1 to 4 m*. Other simulation parameters are according to typical values in Table 5.

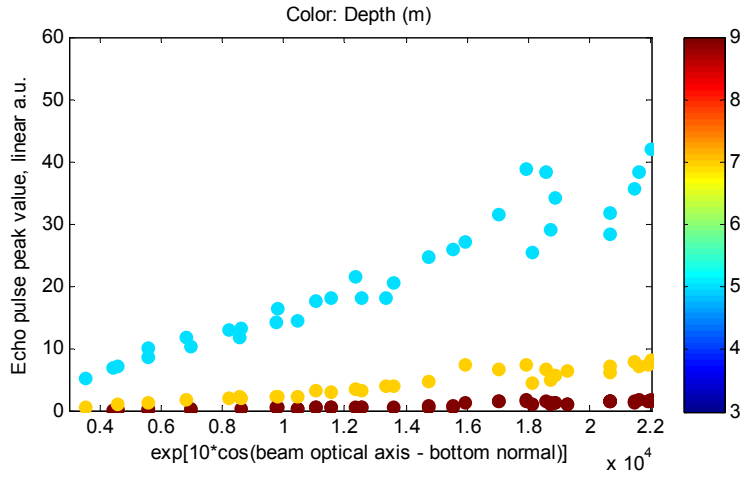

Fig. 16. Simulation results for *echo peak power* with respect to cosine of the angle between bottom normal and the in-water lidar axis unit vector $\hat{\mathbf{n}}_b \cdot \hat{\mathbf{n}}_l$. The bottom slope angle varies between 0° and 20° from the horizontal. With an lidar air off-nadir angle θ_0=20° and a corresponding in-water off-nadir angle $\theta_w \approx 15°$, the maximum angle between bottom normal and lidar optical axis is approximately 35°. Bottom depths 5 m, 7m, and 9 m (colour coded), water attenuation coefficient c = 0.8 m^{-1}, and FOV = 25 mrad. Other simulation parameters are according to typical values in Table 5.

Pulse Area

Simulation results for the bottom echo pulse width are shown in Fig. 17 - Fig. 20. We write the pulse model for the echo pulse area as

$$M_{\text{refl,A}} = C_{\text{A1}} \rho_{532} \frac{\cos^2 \theta_0}{H^2} \exp(-C_{\text{A2}} K_{\text{lidar}} D)(\hat{\mathbf{n}}_b \cdot \hat{\mathbf{n}}_l) + M_{\text{A}}, \qquad (11)$$

where C_{A2} and M_{A} are estimated from a *training data set* of the measured lidar data. The C_{A2} coefficient is set to

$C_{\text{A2}} = 2.5$ for FOV 25 mrad, and

$C_{\text{A2}} = 2$ for FOV 50 mrad,

for bottom depths $D > D_{\text{lim}}$. D_{lim} is set to a default value of 3 m, but this value may be adjusted depending on the water turbidity and other specific conditions in a lidar survey. For bottom depths $D < D_{\text{lim}}$,

$C_{\text{A2}} = 2$ is used for both FOV 25 mrad and 50 mrad.

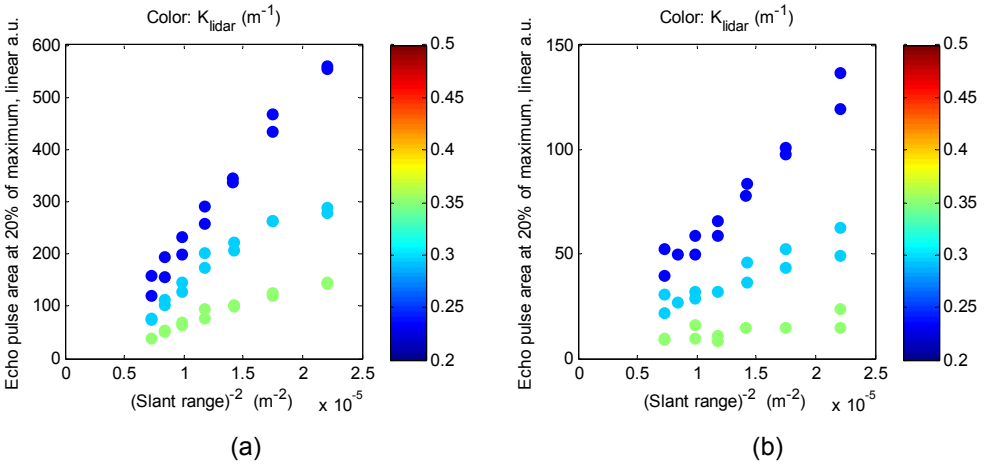

Fig. 17. Simulation results for the *echo pulse area* with respect to inverse squared slant range for bottom depth 5m (a) and 7 m (b). The FOV is 25 mrad and other parameters are according to typical values in Table 5.

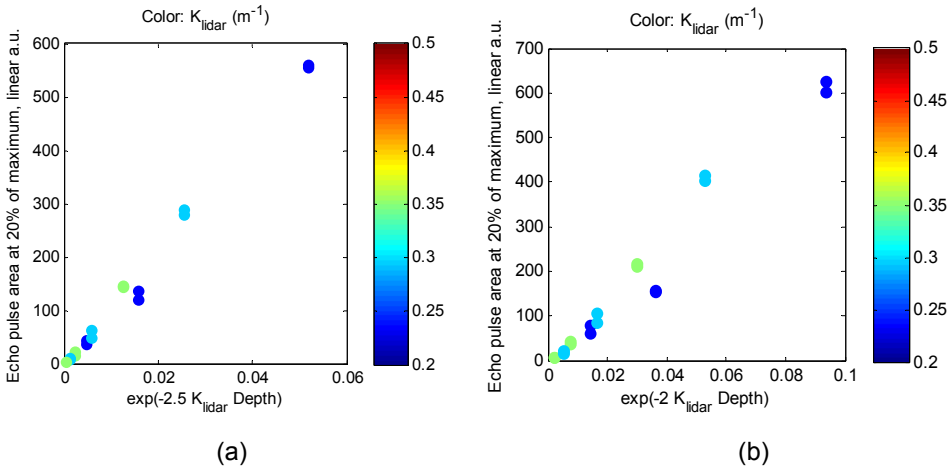

Fig. 18. Simulation results for the *echo pulse area* with respect K_{lidar} and bottom depth for the shallow (a) and deep (b) channels. The bottom depth range is 5 m. Other simulation parameters are according to typical values in Table 5.

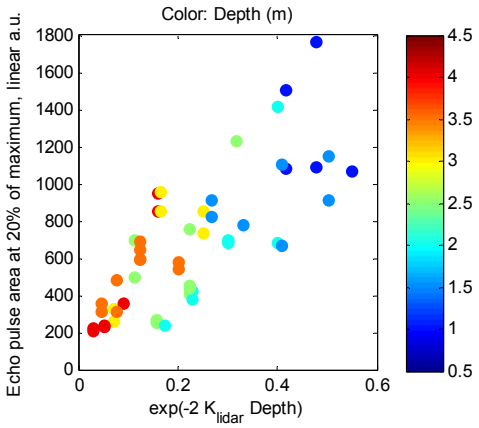

Fig. 19. Simulation results for the *echo pulse area* with respect K_{lidar} and bottom depth for the shallow channel. The bottom depth range is from 1m to 4 m (colour coded). Other simulation parameters are according to typical values in Table 5.

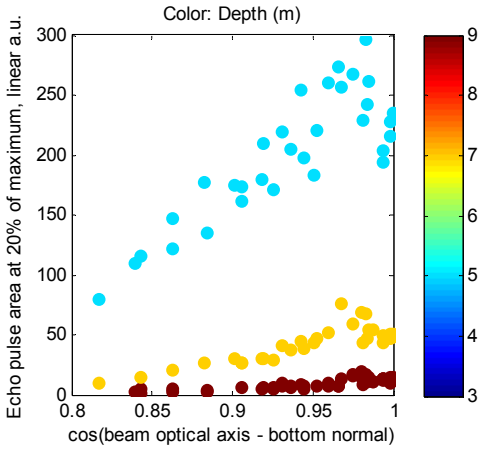

Fig. 20. Simulation results for *echo pulse area* with respect to cosine of the angle between bottom normal and the in-water lidar axis unit vector $\hat{\mathbf{n}}_b \cdot \hat{\mathbf{n}}_l$. The bottom slope angle varies between 0° and 20° from the horizontal. With an lidar air off-nadir angle θ_0=20° and a corresponding in-water off-nadir angle $\theta_w \approx$15°, the maximum angle between bottom normal and lidar optical axis is approximately 35°. Bottom depths 5 m, 7m, and 9 m (colour coded), water attenuation coefficient c = 0.8 m^{-1}, and FOV = 25 mrad. Other simulation parameters are according to typical values in Table 5.

Pulse Width

Simulation results for the bottom echo pulse width are shown in Fig. 21 - Fig. 24. We write the pulse model for the echo pulse width as

$$M_{\text{rough,W}} = C_{\text{W1}} \frac{H}{\cos\theta_0} + C_{\text{W2}} K_{\text{lidar}} + C_{\text{W3}} D + C_{\text{W4}} K_{\text{lidar}} D + C_{\text{W5}} \exp\left[10(\hat{\mathbf{n}}_b \cdot \hat{\mathbf{n}}_l)\right] + M_{\text{W}} \tag{12}$$

for $D > D_{\text{lim}}$.

D_{lim} is set to a default value of 3 m, but this value may be adjusted depending on the water turbidity and other specific conditions in a lidar survey. For small bottom depths, we remove the $C_{\text{W2}}K_{\text{lidar}}$-term and write

$$M_{\text{rough,W}} = C_{\text{W1}} \frac{H}{\cos\theta_0} + C_{\text{W3}} D + C_{\text{W4}} K_{\text{lidar}} D + C_{\text{W5}} \exp\left[10(\hat{\mathbf{n}}_b \cdot \hat{\mathbf{n}}_l)\right] + M_{\text{W}} \tag{13}$$

for $D < D_{\text{lim}}$.

The coefficients C_{W1} - C_{W5}, and M_{W} are estimated from a *training data set* of the measured lidar data. Again, it should be noted that separate and different values for C_{W1} - C_{W5}, and M_{W} are estimated respectively for the shallow and deep channels, and for bottom depths above and below D_{lim}.

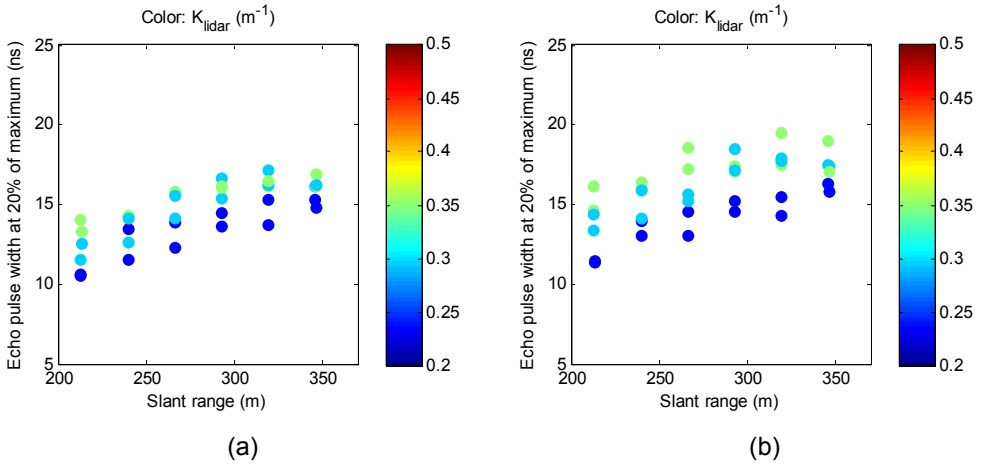

Fig. 21. Simulation results for the *echo pulse width* with respect to slant range $H/\cos\theta_0$ for the shallow (a) and deep (b) channels. The bottom depth is 5 m, and other parameters are according to typical values in Table 5.

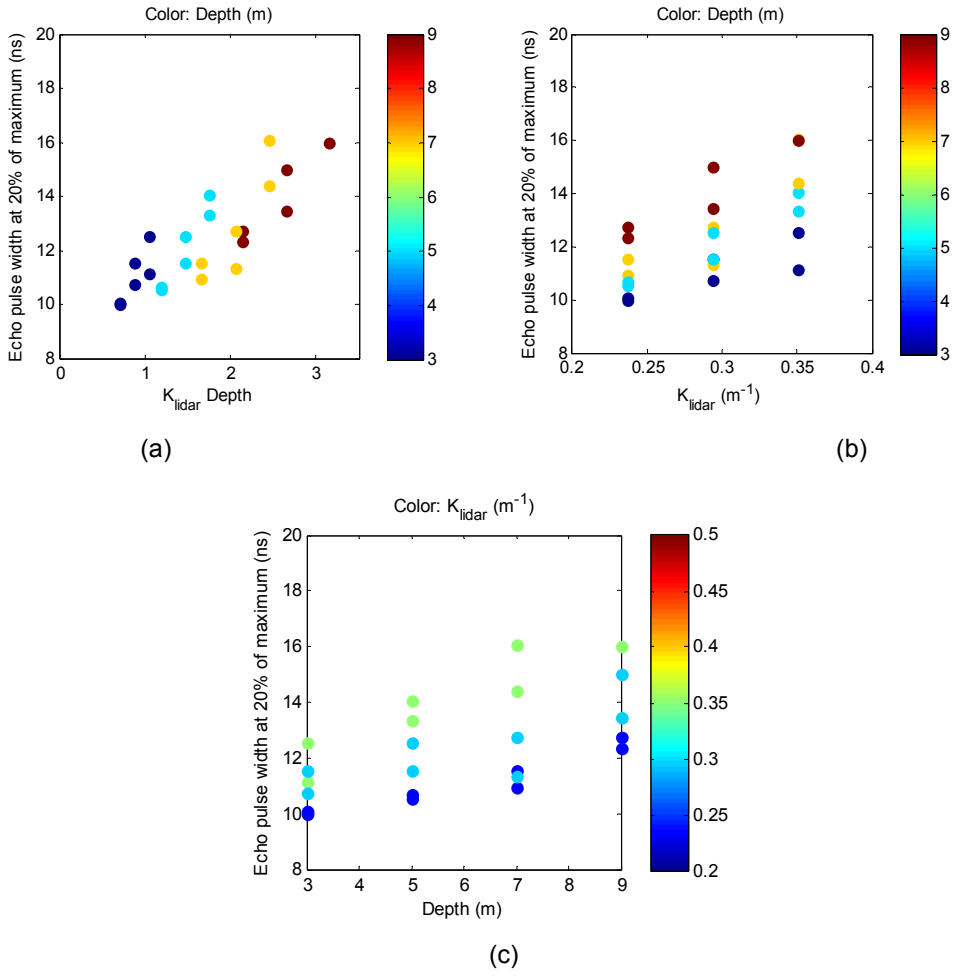

Fig. 22. Simulation results for the *echo pulse width* with respect K_{lidar} and bottom depth (a), K_{lidar} only (b), and depth only (c). Bottom depth range is from 3 m to 9 m. The FOV is 25 mrad and other simulation parameters are according to typical values in Table 5.

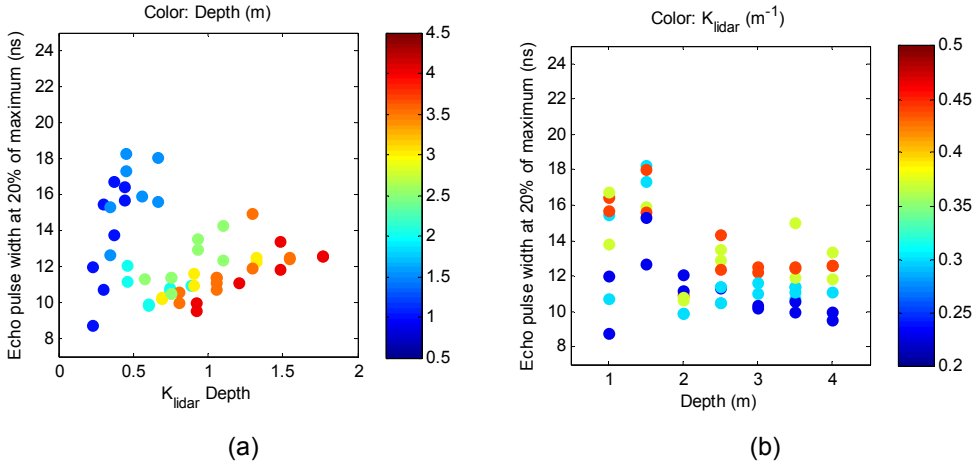

Fig. 23. Simulation results for the *echo pulse width* with respect K_{lidar} and bottom depth (a), and bottom depth only (b). Bottom depth range is from 1 m to 4 m. The FOV is 25 mrad and other simulation parameters are according to typical values in Table 5.

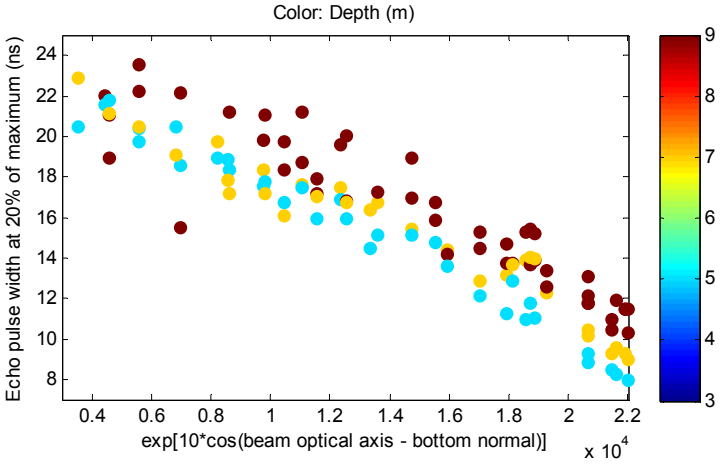

Fig. 24. Simulation results for *echo pulse width* with respect to cosine of the angle between bottom normal and the in-water lidar axis unit vector $\hat{\mathbf{n}}_b \cdot \hat{\mathbf{n}}_l$. The bottom slope angle varies between 0° and 20° from the horizontal. With an lidar air off-nadir angle θ_0=20° and a corresponding in-water off-nadir angle $\theta_w \approx 15°$, the maximum angle between bottom normal and lidar optical axis is approximately 35°. Bottom depths 5 m, 7m, and 9 m (colour coded), water attenuation coefficient c = 0.8 m^{-1}, and FOV = 25 mrad. Other simulation parameters are according to typical values in Table 5.

Pulse leading edge rise time

Simulation results for the bottom pulse rise time are shown in Fig. 25 - Fig. 29. We write the pulse model for the bottom pulse rise time as

$$M_{\text{rough,R}} = C_{\text{R1}} \frac{H^2}{\cos^2 \theta_0} + C_{\text{R2}} K_{\text{lidar}} D + C_{\text{R3}} \left(K_{\text{lidar}} D\right)^2 + C_{\text{R4}} \exp\left[10(\hat{\mathbf{n}}_b \cdot \hat{\mathbf{n}}_l)\right] + M_{\text{R}} \tag{14}$$

for $D > D_{\text{lim}}$.

and

$$M_{\text{rough,R}} = C_{\text{R1}} \frac{H^2}{\cos^2 \theta_0} + C_{\text{R2}} \exp(-2K_{\text{lidar}} D) + C_{\text{R4}} \exp\left[10(\hat{\mathbf{n}}_b \cdot \hat{\mathbf{n}}_l)\right] + M_{\text{R}} \quad (15)$$

for $D < D_{\text{lim}}$.

D_{lim} is set to a default value of 3 m, but this value may be adjusted depending on the water turbidity and other specific conditions in a lidar survey. Separate values for C_{R1} - C_{R4}, and M_{R} are estimated respectively for the shallow and deep channels, and for bottom depths above and below D_{lim}.

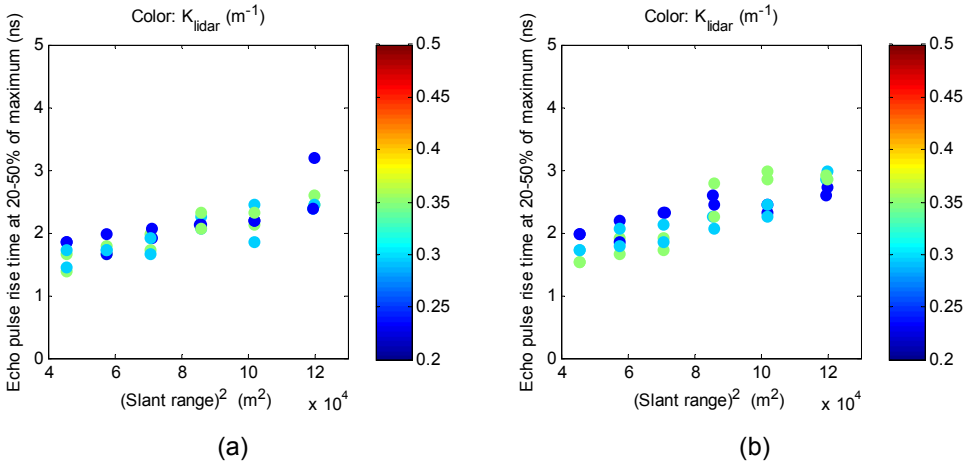

Fig. 25. Simulation results for the *echo pulse rise time* with respect to squared slant range $(H/\cos\theta_0)^2$ for the shallow (a) and deep (b) channels. The bottom depth is 5 m, and other parameters are according to typical values in Table 5.

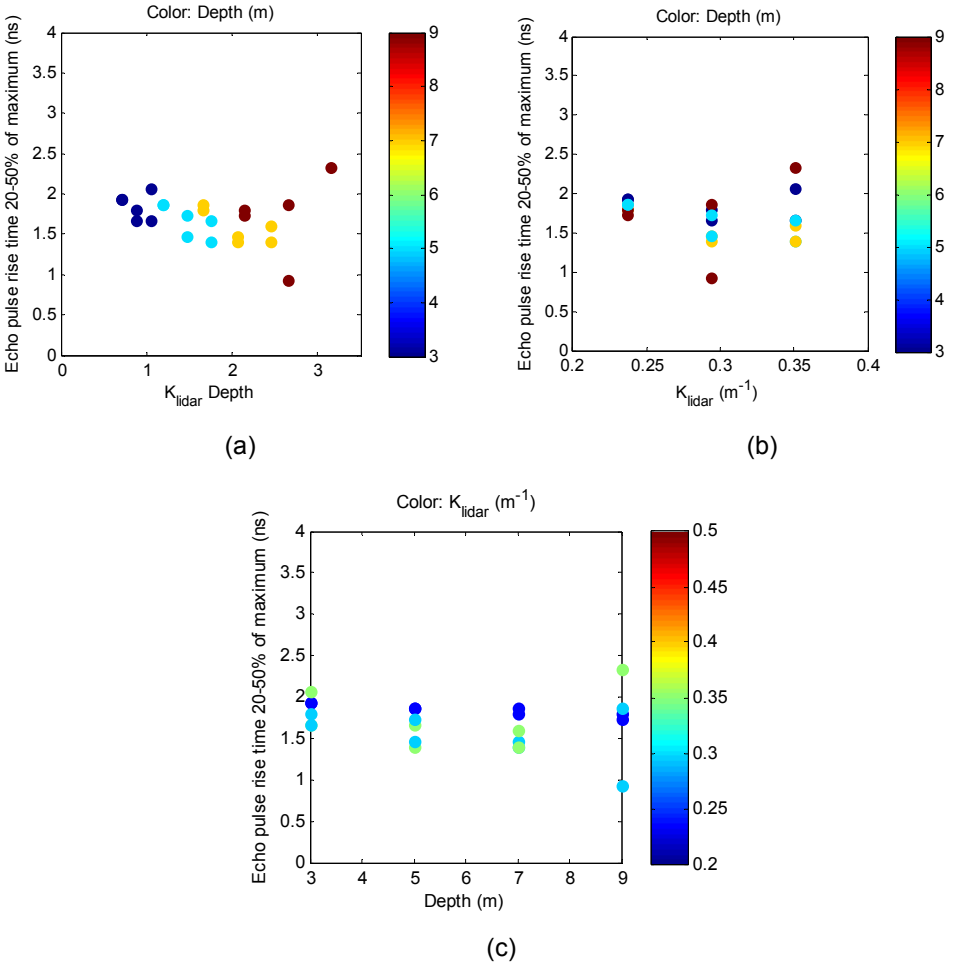

Fig. 26. Simulation results for the *echo pulse rise time* with respect K_{lidar} and bottom depth (a), K_{lidar} only (b), and depth only (c). Bottom depth range is from 3 m to 9 m. The FOV is 25 mrad and other simulation parameters are according to typical values in Table 5.

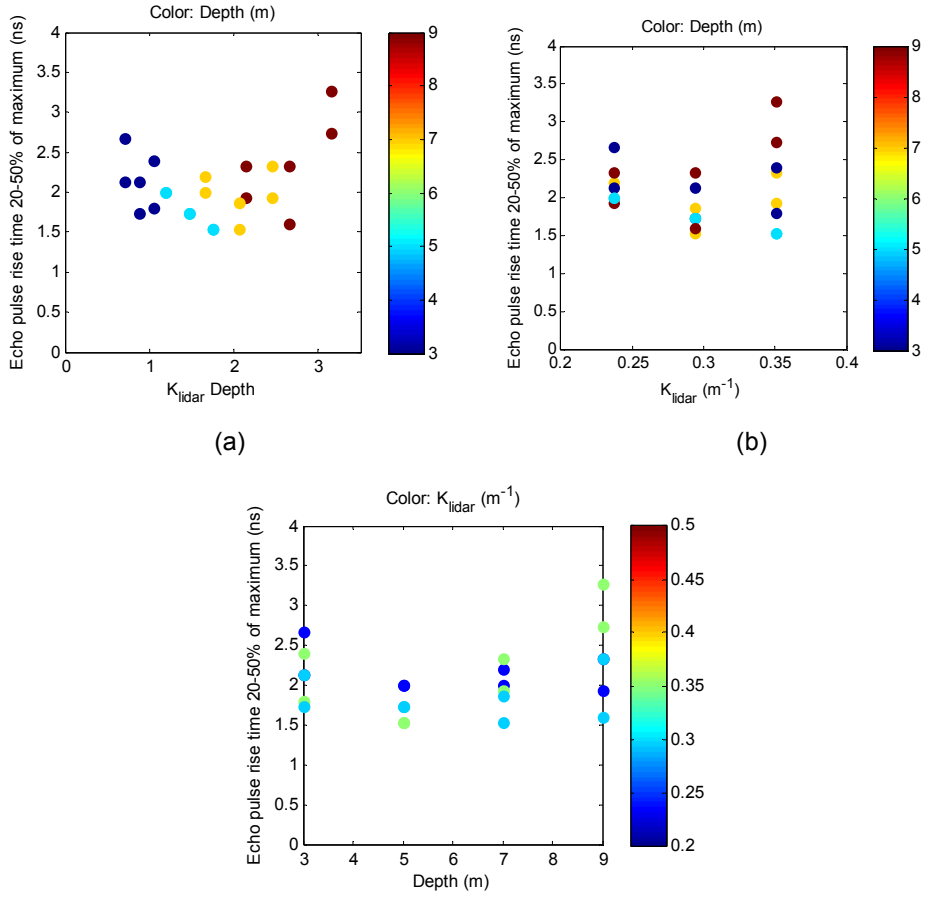

Fig. 27. Similar to Fig. 26 but with FOV=50 mrad. Simulation results for the *echo pulse rise time* with respect K_{lidar} and bottom depth (a), K_{lidar} only (b), and depth only (c). Bottom depth range is from 3 m to 9 m. Other simulation parameters are according to typical values in Table 5.

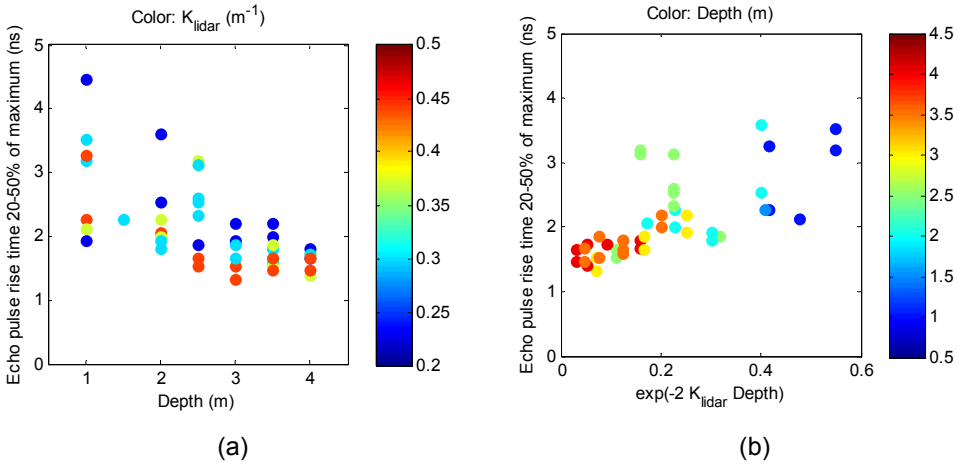

Fig. 28. Simulation results for the *echo pulse rise time* with respect to bottom depth (a), and exponential function of K_{lidar} and bottom depth (b). Bottom depth range is from 1 m to 4 m. The FOV is 25 mrad and other simulation parameters are according to typical values in Table 5.

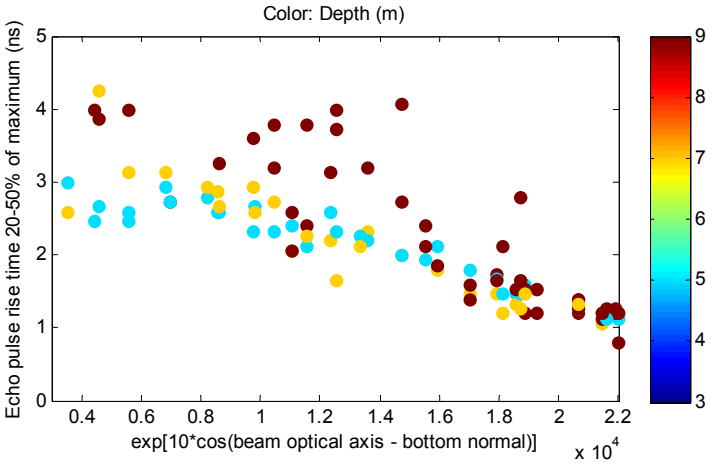

Fig. 29. Simulation results for *echo pulse rise time* with respect to cosine of the angle between bottom normal and the in-water lidar axis unit vector $\hat{\mathbf{n}}_b \cdot \hat{\mathbf{n}}_l$. The bottom slope angle varies between 0° and 20° from the horizontal. With an lidar air off-nadir angle θ_0=20° and a corresponding in-water off-nadir angle $\theta_w \approx 15°$, the maximum angle between bottom normal and lidar optical axis is approximately 35°. Bottom depths 5 m, 7m, and 9 m (colour coded), water attenuation coefficient c = 0.8 m^{-1}, and FOV = 25 mrad. Other simulation parameters are according to typical values in Table 5.

Pulse leading edge derivative

Simulation results for the bottom echo pulse leading edge derivative (from -3 ns to 0 ns relative to the 50% level) are shown in Fig. 30 - Fig. 33. We write the pulse model for the leading edge derivative as

$$M_{\mathrm{mix,D}} = C_{\mathrm{D1}} \rho_{532} \frac{\cos^2 \theta_0}{H^2} \exp(-C_{\mathrm{D2}} K_{\mathrm{lidar}} D) \exp\left[10 \hat{\mathbf{n}}_b \cdot \hat{\mathbf{n}}_l\right] + M_{\mathrm{D}}, \tag{16}$$

where C_{D1} and M_{D} are estimated from the *training data set* of the measured lidar data. The C_{D2} coefficient is set to

$C_{\mathrm{D2}} = 2.5$ for FOV 25 mrad (shallow channel), and

$C_{\mathrm{D2}} = 2$ for FOV 50 mrad (deep channel)

for bottom depths $D > D_{\mathrm{lim}}$. The depth limit D_{lim} is set to a default value of 3 m, but this value may be adjusted depending on the water turbidity and other specific conditions in a lidar survey. For bottom depths $D < D_{\mathrm{lim}}$,

$C_{\mathrm{D2}} = 2$ is used for both FOV 25 mrad and 50 mrad.

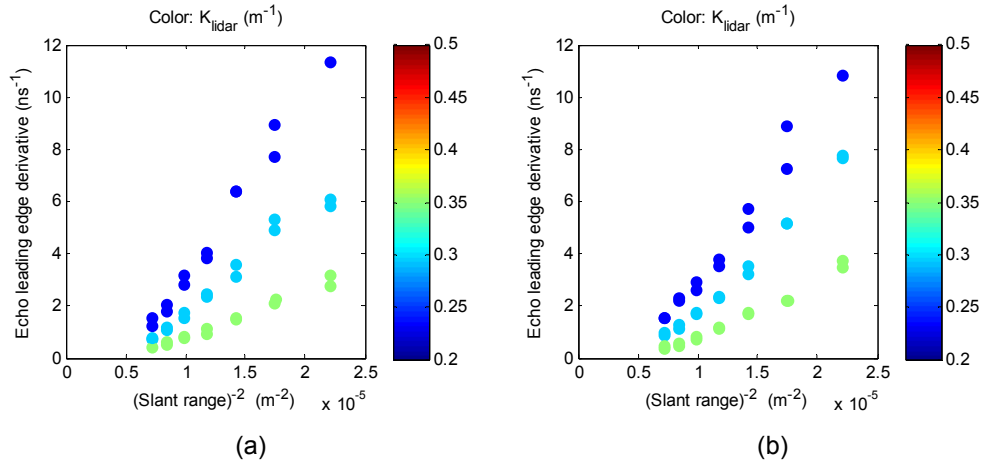

Fig. 30. Simulation results for *echo leading edge derivative* with respect to inverse squared slant range for the shallow (a) and deep (b) channels. The bottom depth is 5 m and other parameters are according to typical values in Table 5.

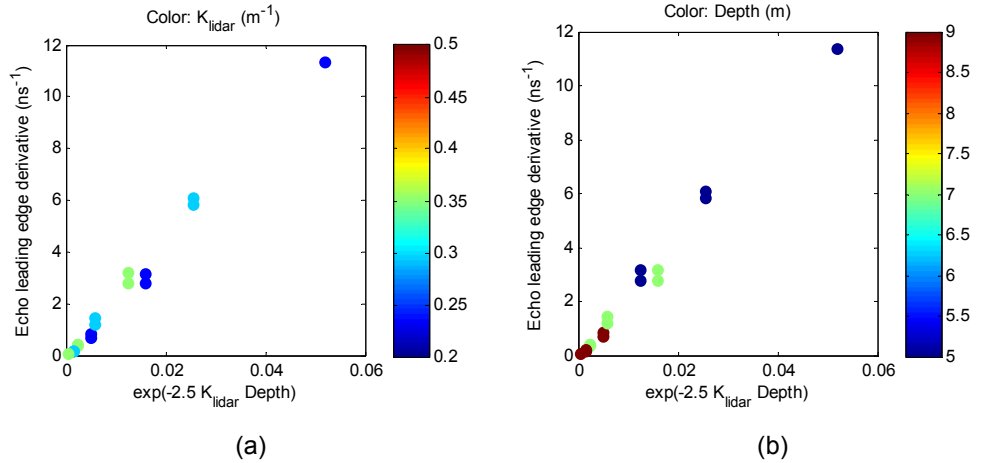

Fig. 31. Simulation results for the *echo leading edge derivative* with respect to an exponential function of K_{lidar} and bottom depth. Colour code: K_{lidar} (a) and depth (b). Bottom depth range is from 5 m to 9 m. The FOV is 25 mrad and other simulation parameters are according to typical values in Table 5.

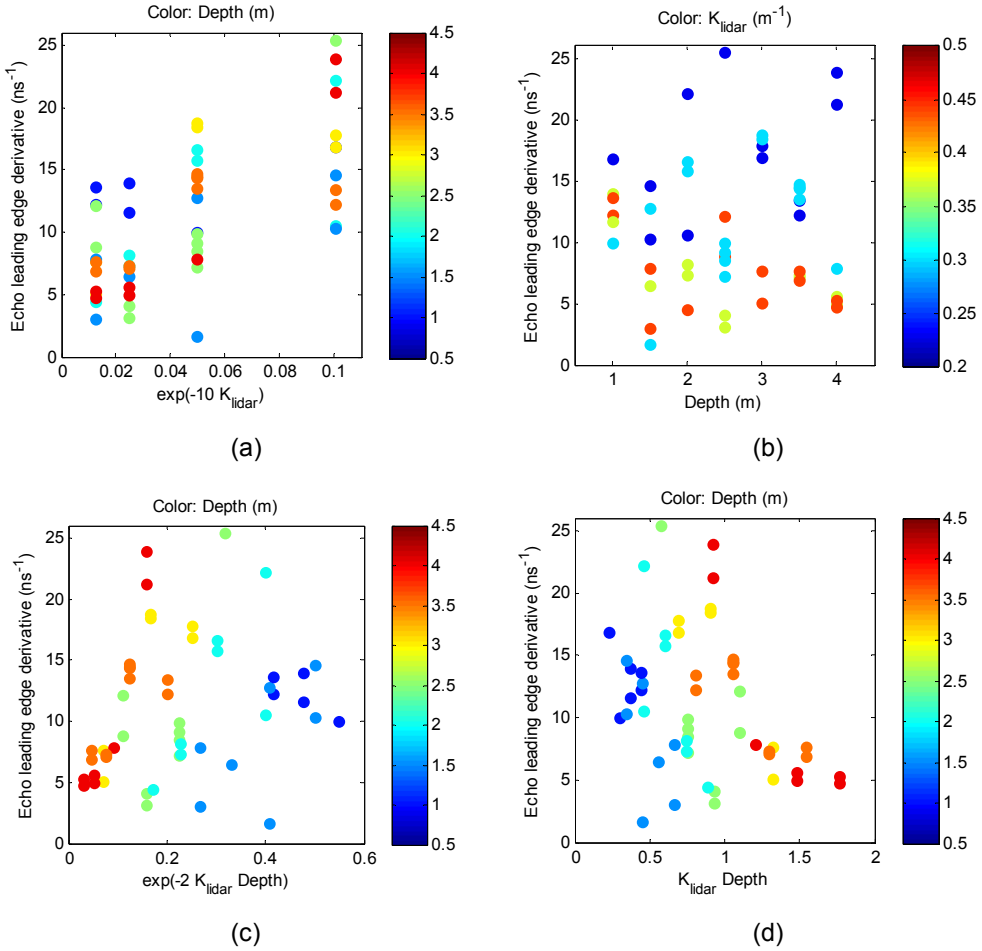

Fig. 32. Simulation results for the *echo leading edge derivative* with respect to an exponential function of K_{lidar} (a), bottom depth (b), exponential K_{lidar} and bottom depth (c), and K_{lidar} and bottom depth (d). Bottom depth range is from 1 m to 4 m. The FOV is 25 mrad and other simulation parameters are according to typical values in Table 5.

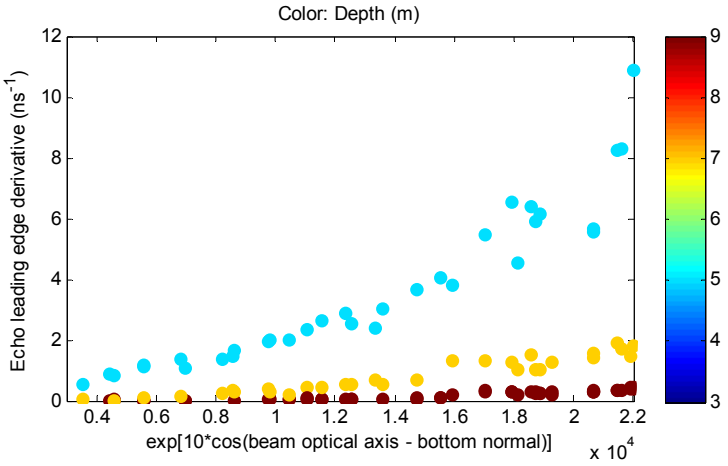

Fig. 33. Simulation results for *echo leading edge derivative* with respect to cosine of the angle between bottom normal and the in-water lidar axis unit vector $\hat{\mathbf{n}}_b \cdot \hat{\mathbf{n}}_l$. The bottom slope angle varies between 0° and 20° from the horizontal. With an lidar air off-nadir angle θ_0=20° and a corresponding in-water off-nadir angle $\theta_w \approx 15°$, the maximum angle between bottom normal and lidar optical axis is approximately 35°. Bottom depths 5 m, 7m, and 9 m (colour coded), water attenuation coefficient c = 0.8 m^{-1}, and FOV = 25 mrad. Other simulation parameters are according to typical values in Table 5.

References

1. V. Méléder, J. Populus, and C. Rollet, "Mapping seabed substrata using Lidar remote sensing," (MESH, 2007).
2. J. Populus, A. Laurentin, C. Rollet, M. Vasquez, B. Guillaumont, and C. Bonnot-Courtois, "Surveying coastal zone topography with airborne remote sensing for benthos mapping," in *EARSeL eProceedings*, *Proc. EARSeL* 3, 1/2004, pp. 105-117, 2004.
3. G. Chust, I. Galparsoro, A. Borja, J. Franco, and A. Uriarte, "Coastal and estuarine habitat mapping, using LIDAR height and intensity and multi-spectral imagery," *Estuarine, Coastal and Shelf Science* **78**, pp. 633-643, 2008.
4. G. Tuell, and J. Y. Park, "Use of SHOALS bottom reflectance images to constrain the inversion of a hyperspectral radiative transfer model," in *Laser Radar and Technology Applications IX*, G. Kamerman, ed., *Proc. SPIE* 5412, pp. 185-193, 2004.
5. G. Tuell, J. Y. Park, J. Aitken, V. Ramnath, V. Feygels, G. Guenther, and Y. Kopilevich, "SHOALS-enabled 3-d benthic mapping," in *Algorithms and Technologies for Multispectral, Hyperspectral, and Ultraspectral Imagery XI*, S. Chen, and P. Lewis, eds., *Proc. SPIE* 5806, pp. 816-826, 2005.
6. C.-K. Wang, and W. D. Philpot, "Using airborne bathymetric lidar to detect bottom type variation in shallow waters," *Remote Sensing of Environment* **106**, pp. 123-135, 2007.
7. H. M. Tulldahl, C. Vahlberg, A. Axelsson, and H. Janeke, "Sea floor characterization from airborne lidar data," in *International Lidar Mapping Forum 08*, *Proc.*, 2008.
8. H. M. Tulldahl, C. Vahlberg, A. Axelsson, H. Karlsson, and P. Jonsson, "Sea floor classification from airborne lidar data," in *Lidar Technologies, Techniques, and Measurements for Atmospheric Remote Sensing III*, U. N. Singh, and G. Pappalardo, eds., *Proc. SPIE* 6750, pp. 675003-675001 -- 675012, 2007.
9. H. M. Tulldahl, and K. O. Steinvall, "Simulation of sea surface wave influence on small target detection with airborne laser depth sounding," *Appl. Opt.* **42**, pp. 2462-2483, 2004.
10. H. M. Tulldahl, and K. O. Steinvall, "Analytical waveform generation from small objects in lidar bathymetry," *Appl. Opt.* **38**, pp. 1021-1039, 1999.
11. O. Steinvall, K. Koppari, U. Lejdebrink, J. Winell, M. Nilsson, R. Ellsén, and E. Gjellan, "Depth sounding lidar-performance and models," in *Laser Radar Technology and Applications*, G. W. Kamerman, ed., *Proc. SPIE* 2748, pp. 18-38, 1996.
12. H. M. Tulldahl, B. Knuthammar, and K. O. Steinvall, "Shoal detection in laser depth sounding," in *Ocean Optics XIV*, S. Ackleson, ed. (Kailua-Kona, Hawaii, 1998).
13. R. G. Congalton, "A review of assessing the accuracy of classifications of remotely sensed data," *Remote Sensing of Environment* **37**, pp. 35-46, 1991.
14. H. M. Tulldahl, B. Knuthammar, and K. O. Steinvall, "Shoal detection in laser depth sounding," in *Ocean Optics XIV*, S. Ackleson, ed., *Proc.*, pp., 1998.
15. K. O. Steinvall, K. R. Koppari, and U. C. M. Karlsson, "Experimental evaluation of an airborne depth-sounding lidar," *Opt. Eng.* **32**, pp. 1307-1321, 1993.
16. G. C. Guenther, and R. W. L. Thomas, "Prediction and correction of propagation-induced depth measurement biases plus signal attenuation and beam spreading for airborne laser hydrography," (NOAA, Rockville, Md., 1984).
17. G. C. Guenther, "Airborne laser hydrography, system design and performance factors," (NOAA, Rockville, Md., 1985).
18. C. D. Mobley, *Light and Water*, Academic Press, San Diego, 1994.
19. J. W. McLean, "Modeling of ocean wave effects for lidar remote sensing," in *Ocean Optics X*, R. W. Spinrad, ed., *Proc. SPIE* 1302, pp. 480-491, 1990.

20. I. L. Katsev, E. P. Zege, A. S. Prikhach, and I. N. Polonsky, "Efficient technique to determine backscattered light power for various atmospheric and oceanic sounding and imaging systems," *J. Opt. Soc. Am.* **14**, pp. 1338-1346, 1997.
21. J. W. McLean, J. D. Freeman, and R. E. Walker, "Beam spread function with time dispersion," *Appl. Opt.* **37**, pp. 4701-4711, 1998.